



**Abstract**

Climate feedbacks over the historical period (1850–2014) have been investigated in large ensembles of historical, hist-ghg, hist-aer, and hist-nat experiments, with 47 members for each experiment. Across the historical ensemble with all forcings, a range in estimated Effective Climate Sensitivity (EffCS) between approximately 3–6 K is found, a considerable spread stemming solely from initial condition uncertainty. The spread in EffCS is associated with varying Sea Surface Temperature (SST) patterns seen across the ensemble due to their influence on different feedback processes. For example, the level of polar amplification is shown to strongly control the amount of sea ice melt per degree of global warming. This mechanism is responsible for the large spread in shortwave clear-sky feedbacks and is the main contributor to the different forcing efficacies seen across the different forcing agents, although in HadGEM3-GC3.1-LL these differences in forcing efficacy are shown to be small. The spread in other feedbacks is also investigated, with the level of tropical SST warming shown to strongly control the longwave clear-sky feedbacks, and the local surface-air-temperatures and large scale tropospheric temperatures shown to influence cloud feedbacks. The metrics used to understand the spread in feedbacks can also help to explain the disparity between feedbacks seen in the historical experiment simulations and a more accurate modeled estimate of the feedbacks seen in the real world derived from an atmosphere-only experiment prescribed with observed SSTs (termed amip-piForcing).

**Plain Language Summary**

Understanding how the Earth’s climate responds to an imposed forcing such as an increase in greenhouse gases or aerosols is an important issue relevant to climate mitigation and adaptation policies on the global scale. One way we can understand this is by analysing the historical period (1850–2014), a period over which the climate has already changed substantially due to human induced forcings, and also a period over which observations allow us to compare modeled changes in climate with the changes seen in the real world. Here, we use a large ensemble of climate model simulations of the historical period where we aim to understand a) how natural variability causes differences in the global temperature response to the same imposed forcing, b) what causes different forcing agents (e.g. greenhouse gases or aerosols) to be more or less effective at warming or cooling the planet, and c) whether historical simulations - where the climate model simulates its own sea surface temperatures - capture the same response to historical forcings as an atmosphere-only simulation prescribed with observed sea surface temperatures. We find that the pattern of sea surface temperatures (particularly the levels of tropical and polar warming) is key to understanding each of these points.

**1 Introduction**

Climate sensitivity and feedbacks provide valuable information about how the Earth’s temperature changes in response to an imposed forcing such as an increase in greenhouse gases, aerosols, or volcanic emissions (Sherwood et al., 2020; Forster et al., 2021). Typically, equilibrium climate sensitivity (ECS) is defined as the equilibrium global temperature increase in response to a doubling of CO<sub>2</sub> and can be related to CO<sub>2</sub> forcing and climate feedbacks using a simple energy balance model (Equation 1) (e.g. Sherwood et al. (2020)).

$$ECS = -F_{2\times CO_2}/\lambda \quad (1)$$

Here,  $F_{2\times CO_2}$  is the radiative forcing associated with a doubling of CO<sub>2</sub> and the feedback parameter  $\lambda$  is the radiative response per degree of global temperature change. Currently, the assessed likely range of ECS extends from 2.5°C – 4.0°C (Forster et al.,

2021). Since constraining ECS is important for improving our understanding of how the Earth’s climate is likely to change in the future, informing climate related mitigation and adaptation policy on the global scale, improving our understanding of different climate feedbacks and why they vary is vital.

The feedback parameter  $\lambda$  can be defined using Equation 2 (e.g. Gregory et al. (2004)).

$$\lambda = d(N - F)/dT_s \quad (2)$$

Here  $F$  is the radiative forcing,  $N$  is the top of atmosphere radiative flux, and  $T_s$  is the surface-air-temperature (in this case, all terms are global mean quantities).

In Atmosphere-Ocean General Circulation Models (AOGCMs),  $\lambda$  and ECS are typically estimated via a linear regression of global  $T_s$  and  $N$  over the first 150 years of an abrupt-4xCO<sub>2</sub> simulation (T. Andrews et al., 2012; Dong et al., 2021; Gregory et al., 2004). The abrupt-4xCO<sub>2</sub> simulation is an AOGCM experiment where the atmospheric concentration of CO<sub>2</sub> is abruptly quadrupled and then held constant. This regression method is used in favour of calculating ECS directly from two equilibrium states due to the long timescales needed to equilibrate the deep ocean and the substantial computational cost associated with this (T. Andrews et al., 2022; Rugenstein et al., 2019). ECS estimates produced from these non-equilibrium states are called the Effective Climate Sensitivity (EffCS) (Dong et al., 2021; Sherwood et al., 2020; T. Andrews et al., 2015; Rugenstein & Armour, 2021).

$\lambda$  and EffCS can also be estimated from simulations of the historical record (1850 to present day), estimating  $\lambda$  over the historical period and applying this to Equation 1 where  $F_{2\times CO_2}$  has been diagnosed from an abrupt-4xCO<sub>2</sub> run (Gregory et al., 2020). These estimates tend to produce an EffCS smaller than that predicted solely from an abrupt-4xCO<sub>2</sub> experiment, largely due to the time variations in  $\lambda$  caused by evolving SST patterns and the different timescales involved in the response to an imposed forcing (T. Andrews et al., 2019; Gregory et al., 2020; Proistosescu & Huybers, 2017). This “pattern effect” describes how a different global radiative response can be generated by the same global temperature change due to different patterns of SSTs (Rugenstein & Armour, 2021; Gregory & Andrews, 2016). In this context, the pattern effect is often quantified as the difference in  $\lambda$  between historical and abrupt-4xCO<sub>2</sub> experiments (T. Andrews et al., 2018).

Estimates of  $\lambda$  from historical and abrupt-4xCO<sub>2</sub> simulations may also differ due to the different forcing agents involved (Marvel et al., 2015). Whilst the abrupt-4xCO<sub>2</sub> experiment is only forced by increases in CO<sub>2</sub> concentrations, the historical simulations are also influenced by changes in aerosols and natural forcings such as volcanic emissions (C. J. Smith & Forster, 2021; Salvi et al., 2023). These different forcing agents may vary in how effective they are at warming or cooling the planet; this is called forcing efficacy (Marvel et al., 2015; Richardson et al., 2019; Hansen et al., 2005). Again AOGCMs can be used to investigate this, with experiments simulating the historical period but only applying the forcing for individual forcing agents. Salvi et al. (2022) use this approach to demonstrate that, in the multi-model mean, greenhouse gases tended to have a more stabilising feedback (lower EffCS) compared to aerosols, although substantial variation across different models exists. It is suggested that across different forcing agents, variations in SST pattern changes lead to differing feedbacks (Haugstad et al., 2017). Ceppi and Gregory (2019) suggest that the changes in atmospheric stability induced by these differing SST patterns is a key factor determining the efficacy of a particular forcing (Salvi

108 et al., 2023). Assuming temperature changes and the radiative responses to each forc-  
109 ing agent add linearly, understanding each component of the full historical forcing can  
110 help inform our interpretation of historical feedbacks and how they relate to future cli-  
111 mate change.

112 Historical estimates of a model’s EffCS can also be deduced from an Atmosphere  
113 only General Circulation Model (AGCM) experiment with prescribed SSTs and sea ice  
114 from observations between 1870 and 2014 and atmospheric constituents set to pre-industrial  
115 levels, termed amip-piForcing (Gregory & Andrews, 2016; Gregory et al., 2020). Because  
116 this experiment is forced with observed SSTs it is able to more accurately simulate his-  
117 torical changes in climate compared to the coupled AOGCMs (Gregory & Andrews, 2016).  
118 It is found that the EffCS calculated using the amip-piForcing experiment tends to pro-  
119 duce an EffCS smaller than that derived from AOGCM historical experiments (i.e. amip-  
120 piForcing has a larger pattern effect relative to abrupt-4xCO<sub>2</sub>) (Gregory et al., 2020; T. An-  
121 drews et al., 2019). Again, this difference is often attributed to differences in SST pat-  
122 terns between the two experiments, with coupled historical simulations struggling to sim-  
123 ulate observed SST patterns (Gregory et al., 2020; Wills et al., 2022). Over recent years,  
124 observed SSTs demonstrate a marked cooling in the East Pacific and Southern Ocean  
125 and more warming over the West Pacific, leading to more negative feedbacks and a lower  
126 EffCS. The inability of AOGCM simulations to capture observed trends in SST patterns  
127 is a key issue currently facing the scientific community and raises questions regarding  
128 how this impacts our understanding of climate sensitivity and feedbacks. The “peculiar”  
129 trend in SST patterns as termed by Fueglistaler and Silvers (2021) may have occurred  
130 through unforced variability and it may then be by chance that the real world SSTs have  
131 evolved in a way that induces a more strongly stabilising feedback. Or, it is possible that  
132 the trend is forced, e.g. by aerosols or volcanic emissions (D. Smith et al., 2016; Gregory  
133 et al., 2020; Hwang et al., 2024), and our AOGCMs struggle to simulate the real world  
134 SSTs accurately due to limitations in our current modelling capabilities.

135 To date, most of the work examining radiative feedbacks, pattern effects and ef-  
136 ficacies has been limited to idealised experimental designs or small ensembles of histor-  
137 ical AOGCM simulations with a single model, or via model intercomparisons such as the  
138 Coupled Model Intercomparison Project (CMIP) (Eyring et al., 2016), where still only  
139 relatively small ensemble sizes are available. Questions remain on the influence of nat-  
140 ural variability in historical climate change on diagnosed estimates of feedbacks, the quan-  
141 tification of the forced response to different forcings and whether radiative feedback sim-  
142 ulated in AOGCM historical simulations are consistent with observed estimates. Large  
143 initial condition ensembles with a single model are useful to address this. For example,  
144 previously, large ensembles have been shown to provide valuable insight into the sepa-  
145 ration of forced climate change and internal variability (Kay et al., 2015). From a sea  
146 ice sensitivity perspective, Kay et al. (2011) demonstrate that using an ensemble to quan-  
147 tify internal variability shows that recent trends in sea ice decline cannot be reproduced  
148 from modeled internal variability alone. Adams and Dessler (2019) employ a 100 mem-  
149 ber ensemble of historical simulations to show that internal variability could be a key  
150 contributor to the difference in Transient Climate Response (TCR) estimates between  
151 models and observations. Applying the analysis of this 100 member ensemble to the study  
152 of climate sensitivity and feedbacks over the historical period, Dessler et al. (2018) high-  
153 light a large range in EffCS estimates between 2.1 and 3.9K. They note that given that  
154 the real world 20<sup>th</sup> century is just one realisation of a range of possible realities, due to  
155 that large internal variability, we should not expect estimates of EffCS from observations  
156 to be a precise guide to the real world’s forced response. Alongside this, they note that  
157 that different forcing efficacies, imperfect observations, and uncertainty in 20th century  
158 forcing also pose challenges for interpreting EffCS from the historical period. Gregory  
159 et al. (2020) also noted the high levels of internal variability over the historical record  
160 showing how this variability contributed to uncertainty to estimates of EffCS.

161 In this paper we use a new set of four large ensembles of HadGEM3-GC3.1-LL his-  
 162 torical and single forcing simulations performed for the Large Ensemble Single Forcing  
 163 Model Intercomparison Project (LESFMIP) (D. Smith et al., 2022), aiming to address  
 164 the following questions.

- 165 1. how does natural variability cause differences and spread in climate feedbacks in  
 166 response to the same imposed forcing?
- 167 2. What causes different efficacies of different historical forcing agents?
- 168 3. Can AOGCM historical simulations – where the model simulates it’s own SSTs  
 169 - capture the radiative feedback and EffCS estimated from AGCM experiments  
 170 prescribed with observed SSTs?

171 Previously, T. Andrews et al. (2019) investigated EffCS and feedbacks in HadGEM3-  
 172 GC3.1-LL in a 4 member ensemble of historical simulations, finding a net feedback ( $\lambda$ )  
 173 of  $-0.86 \pm 0.4 \text{ Wm}^{-2}\text{K}^{-1}$  (5-95%). This ensemble mean estimate is more negative than  
 174 the abrupt-4 $\times$ CO<sub>2</sub> feedback in HadGEM3-GC3.1-LL of  $-0.63 \text{ Wm}^{-2}\text{K}^{-1}$ , although the  
 175 5-95% confidence range does extend up to  $-0.46 \text{ Wm}^{-2}\text{K}^{-1}$ . The large spread in  $\lambda$  was found  
 176 to be partly caused by considerable variations in Antarctic sea ice. This variability in  
 177 sea ice inhibited accurate evaluation of the model’s historical forced EffCS. There, T. An-  
 178 drews et al. (2019) were limited to an ensemble of only 4 simulations, so questions re-  
 179 main about whether the full diversity of variability was sampled. Here we investigate this  
 180 with a much larger ensemble of 47 members.

181 In the following section we describe the model and experimental setup used. Sec-  
 182 tion 3 presents the results and Section 4 provides a discussion and conclusions.

## 183 2 Methods

### 184 2.1 HadGEM3-GC3.1-LL

185 The analysis in this paper uses simulations performed using HadGEM3-GC3.1-LL,  
 186 an AOGCM with an atmospheric resolution of 135 km with 85 vertical levels and an ocean  
 187 resolution of 1° and 75 vertical levels (M. B. Andrews et al., 2020). Further details can  
 188 be found in Williams et al. (2017) where a description of the model’s configuration is given.

### 189 2.2 Large Historical Ensemble

190 In this analysis, ensembles of historical, hist-ghg, hist-aer, and hist-nat experiment  
 191 are used, with 47 members of each experiment mostly consisting of simulations performed  
 192 for LESFMIP. These experiments are AOGCM simulations analysed between 1850–2014  
 193 with atmospheric constituents set to historical levels. Here, the historical experiment in-  
 194 cludes all forcing agents, whilst the hist-ghg, hist-aer, and hist-nat contain only the forc-  
 195 ing associated with well mixed greenhouse gases, anthropogenic aerosols, and natural forc-  
 196 ings respectively (Gillett et al., 2016). Each ensemble member differs only in their ini-  
 197 tial conditions branching from the piControl experiment at different times (1850, 1885,  
 198 and every 10 years between 1860 and 2300). The piControl experiment is an AOGCM  
 199 experiment with atmospheric constituents set to pre-industrial levels. The 47 ensemble  
 200 members consist of 45 simulations performed as part of the LESFMIP ensemble (D. Smith  
 201 et al., 2022), and two simulations previously analysed in T. Andrews et al. (2019). Only  
 202 two of the four simulations used in T. Andrews et al. (2019) were analysed here since  
 203 the other two members had identical branch times to members of the LESFMIP ensem-  
 204 ble.

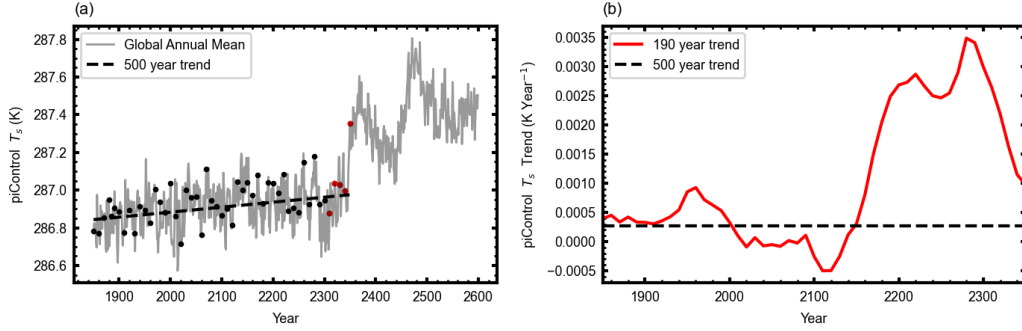


**Figure 1.** (a) Timeseries of global annual mean  $T_s$  in the piControl experiment (grey line), 500 year trend (dashed black line), and branch times for each of the historical and single forcing experiment ensemble members (dots). Red dots indicate the ensemble members that have been excluded due to the strong warming seen in the piControl experiment. (b) 190 year piControl trend for each ensemble member branch date (red), and 500 year piControl trend (horizontal black dashed line).

205

### 2.3 piControl and Detrending

206

207

208

209

210

211

212

213

214

215

216

217

218

219

220

221

222

223

224

225

226

227

228

229

To compare ensemble members in the 47 member ensembles, the control drift must be removed from each simulation. For this analysis, this drift is removed by calculating the trend over the first 500 years of the piControl experiment via linear regression and subtracting the corresponding time period from each ensemble member. The piControl timeseries of global annual mean  $T_s$  and the 500 year trend is shown in Figure 1a where the dots depict the branch dates for each member of the historical ensemble. This method of control drift removal is chosen in favour of subtracting the piControl year by year to avoid unnecessarily introducing more noise into the historical simulations. The 500 year trend is also preferred above subtracting the 190 year trend across the corresponding piControl period due to issues introduced towards the end of the piControl simulation, where a marked global warming is seen at around 2350. This warming has been previously documented by Ridley et al. (2022) where it is attributed to the onset of deep convection in the Weddell and Ross Sea gyres due to a destabilising of the Southern Ocean. When removing the control drift from the historical ensemble, any drift removed is assumed to be present in the historical ensemble member. For the trend seen over the first 500 years of the control run this is a reasonable assumption, however in the case of the large warming seen around 2350, this assumption may not hold. The impact that this warming has on the 190 year control trend for the respective historical ensemble branch dates is shown in Figure 1b. Here, unsurprisingly, a strong positive trend is seen for ensemble members that branch after the year 2150. We found no evidence that the warming seen in the piControl experiment is present in historical ensemble members initiated up to 2300, but to avoid this feature contaminating the comparison of ensemble members, the last 5 ensemble members have been removed from the analysis. This is why although the LESFMIP ensemble consists of 50 members, only 45 of them are used here.

230

### 2.4 Diagnosing Historical Forcing

231

232

233

Whilst  $\lambda$  can be calculated for the abrupt-4xCO2 and amip-piForcing experiments from only  $T_s$  and  $N$  (since the  $F$  is constant), the time varying  $F$  over the historical period means that in order to estimate  $\lambda$ , we must first diagnose  $F$ .

**Table 1.** Description of experimental setup used.

Experiments				
Experiment Name	Atmospheric Constituents	SSTs	Run Time	Ensemble Size
Coupled experiments				
piControl	pre-industrial	free running	1850 – 3850	1
abrupt-4xCO2	pre-industrial CO <sub>2</sub> ×4	free running	1850 – 2350	1
historical	historical	free running	1850–2014	47
hist-ghg	historical well mixed greenhouse gases	free running	1850–2014	47
hist-aer	historical aerosols	free running	1850–2014	47
hist-nat	historical natural forcing	free running	1850–2014	47
Atmosphere-only experiments				
amip-piForcing	pre-industrial	historical observed	1870 – 2014	1
piClim-control	pre-industrial	piControl	1850 – 1890	3
piClim-histall	historical to 2014 then ssp-245 to 2100	piControl	1850 – 2100	3
piClim-histghg	historical well mixed greenhouse gases only to 2014 then ssp-245 to 2100	piControl	1850 – 2100	3
piClim-histaer	historical aerosols only to 2014 then ssp-245 to 2100	piControl	1850 – 2100	3
piClim-histnat	historical natural forcing only to 2014 then ssp-245 to 2100	piControl	1850 – 2100	3

234 Typically, the historical  $F$  is diagnosed using RFMIP experiments piClim-control  
235 and piClim-histall (Forster et al., 2016; Pincus et al., 2016). These are two AGCM ex-  
236 periments with prescribed SSTs from the piControl simulation. For piClim-control, at-  
237 mospheric constituents are set to pre-industrial levels and the experiment is run for 30  
238 years. Averaging over the 30 years provides the control state. For piClim-histall atmo-  
239 spheric constituents are set to historical levels between 1850 – 2014 and to ssp-245 lev-  
240 els between 2015 and 2100. Subtracting the 30 year mean piClim-control top of atmo-  
241 sphere radiative flux from the 1850 – 2100 piClim-histall top of atmosphere flux provides  
242  $F$ , with years 1850–2014 relevant for the analysis of the historical period.

243 In order to diagnose  $F$  for the individual forcing components that correspond to  
244 the hist-ghg, hist-aer, and hist-nat experiments, a similar experimental setup to the piClim-  
245 histall experiment is used but only the forcing from the relevant component is applied.  
246 These experiments are termed piClim-histghg, piClim-histaer, and piClim-histnat (Forster  
247 et al., 2016; Pincus et al., 2016).

248 A summary of the setup for each experiment used in this paper is presented in Ta-  
249 ble 1.

### 3 Results

#### 3.1 Diagnosing Feedbacks in Historical and Single Forcing Ensembles

As discussed in the introduction, the feedback parameter ( $\lambda$ ) can be estimated via linear regression of global annual mean surface-air-temperatures ( $T_s$ ) against top of atmosphere radiative fluxes ( $N$ ) minus the changes in flux associated with the radiative forcing ( $F$ ). Timeseries of these diagnostics are presented in Figure 2, where 2a and b show the anomalous global annual mean  $T_s$  and anomalous global annual mean  $N$  respectively in every ensemble member and in each experiment, and 2c shows the global annual mean  $F$  associated with each experiment. From Figure 2a it can be seen that the cooling effect of anthropogenic aerosols and natural forcings is approximately offset by the warming effect of increased greenhouse gases between 1850 and 1990. Here, the  $F$  associated with greenhouse gases and aerosols gradually increase, however, after approximately 1990 the aerosol  $F$  remains relatively constant (around  $-1.5 \text{ Wm}^{-2}$ ) whilst the  $F$  associated with greenhouse gases continues to increase (Figure 2c) (T. Andrews et al., 2019). This leads to a net positive  $F$  after 1990 in the historical experiment which results in an increase in global mean  $T_s$ , warming by approximately 0.8 K by 2014. A detailed analysis of HadGEM3-GC3.1-LL historical simulations is presented in M. B. Andrews et al. (2020). An example of how  $\lambda$  is calculated from these timeseries of  $T_s$ ,  $N$ , and  $F$  is presented in Figure 2d, where, for the first ensemble member in the historical experiment, a feedback parameter of  $-0.85 \pm 0.15 \text{ Wm}^{-2}\text{K}^{-1}$  is estimated. There the uncertainty is estimated as  $\pm 1.645$  standard deviations, calculated from the standard error of the linear fit.

One assumption made when estimating  $\lambda$  using timeseries of  $T_s$ ,  $N$ , and  $F$  is that the changes in global mean  $T_s$  associated with the forcing is zero (i.e. the surface-air-temperature change between piClim-control and piClim-histall is zero). This is generally a reasonable assumption to make, given that the prescribed SSTs do not warm and therefore any changes in land surface temperatures are constrained to be small (Lambert et al., 2011). However, despite this temperature change being small, taking this into account can substantially affect the values of  $\lambda$  estimated. This caveat is noted in Hansen et al. (2005) and Vial et al. (2013) and becomes a particularly relevant issue when comparing feedbacks in the historical experiment to feedbacks in the amip-piForcing experiment, since there is no forced temperature change in the amip-piForcing experiment where  $F = 0$  by construction. To handle this issue, in this paper,  $\lambda$  has been calculated accounting for this forced temperature change (Equation 3).

$$\lambda = d(N - F)/d(T_s - \delta T_{s_{forced}}) \quad (3)$$

Where  $\delta T_{s_{forced}}$  is calculated as the change in global surface-air-temperature between piClim-control and the relevant piClim-hist experiment used to diagnose  $F$ . To simplify the notation, we refer to  $(T_s - \delta T_{s_{forced}})$  simply as  $T_s$ . Similarly, later when analysing atmospheric temperatures ( $T_a$ ), we refer to  $(T_a - \delta T_{a_{forced}})$  simply as  $T_a$ .

To summarise the feedbacks seen across the different experiments analysed, box-plots of feedbacks in the historical and single forcing experiments and markers showing the feedbacks in both amip-piForcing and abrupt-4xCO2 experiments are shown in Figure 3b. Here the net feedback has been decomposed into shortwave clear-sky ( $SW_{cs}$ ), longwave clear-sky ( $LW_{cs}$ ), and cloud radiative effect ( $cre$ ) components. Such a decomposition is useful since it can help isolate the different processes and feedback mechanisms involved.  $\lambda_{SW_{cs}}$ ,  $\lambda_{LW_{cs}}$ , and  $\lambda_{cre}$  are calculated by decomposing  $N$  and  $F$  into the relevant fluxes when applying Equation 3. From Figure 3b, a large spread in feedbacks across the historical ensemble can be seen, ranging from approximately  $-0.7$  to  $-1.3 \text{ Wm}^{-2}\text{K}^{-1}$ . Using a  $2 \times \text{CO}_2$   $F$  of  $4.05 \text{ Wm}^{-2}$  for HadGEM3-GC3.1-LL (T. Andrews

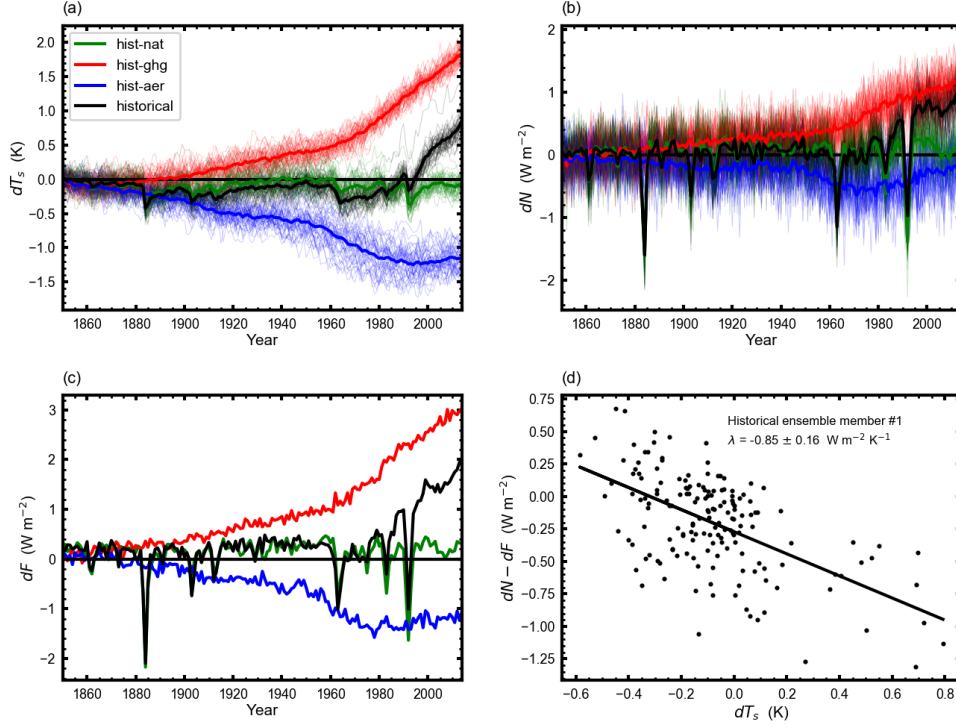


**Figure 2.** (a) Timeseries of anomalous global annual mean  $T_s$  in the historical and single forcing experiments. Thick lines indicate the ensemble mean and thinner lines represent each individual ensemble member. (b) Timeseries of anomalous global annual mean  $N$  in the historical and single forcing experiments. Again, thick lines indicate the ensemble mean and thinner lines represent each individual ensemble member. (c) Timeseries of global annual mean  $F$  for historical and single forcing scenarios averaged across the three ensemble members for each experiment. (d) Example of method used to estimate  $\lambda$ , where  $\lambda$  is calculated by linearly regressing  $T_s$  against  $(N - F)$ . Each dot represents a year in the historical experiment and the black line shows regression line where the slope ( $\lambda$ ) is estimated to be  $-0.85 \pm 0.15 \text{ W m}^{-2} \text{ K}^{-1}$ . Here, the uncertainty is estimated as  $\pm 1.645$  standard deviations, calculated from the standard error of the linear fit.

299 et al., 2019), and applying Equation 1, such a range in feedbacks leads to an estimate  
 300 of EffCS between approximately 3 and 6K (Figure 3a). This highlights the role of in-  
 301 ternal variability in causing different feedback and EffCS estimates over the historical  
 302 period. The spread in feedbacks seen in the historical and single forcing experiments is  
 303 largest in the hist-nat experiment and smallest in the hist-ghg experiment, possibly due  
 304 to the varying signal to noise ratios across the different experiments. The  $T_s$  changes in  
 305 the hist-nat experiment are generally small (Figure 2a), and the natural  $F$  is also small  
 306 with an occasional strong but short-lived signal caused by volcanic emissions (Figure 2c).  
 307 This causes the regression of  $T_s$  against  $(N - F)$  to be relatively noisy compared to the  
 308 hist-ghg experiment where both  $T_s$  and  $(N - F)$  have a much stronger signal. This is  
 309 also consistent with the contrast in estimated uncertainty of the linear fit of  $T_s$  and  $(N -$   
 310  $F)$  where for each experiment, the standard error of the linear fit of every ensemble member  
 311 has been estimated. The estimation of  $\lambda_{net}$  in the hist-ghg experiment has an average  
 312 5-95% interval of  $\pm 0.066 \text{ W m}^{-2} \text{ K}^{-1}$ , whereas for hist-nat, the mean 5-95% interval is  
 313  $\pm 0.25 \text{ W m}^{-2} \text{ K}^{-1}$ .

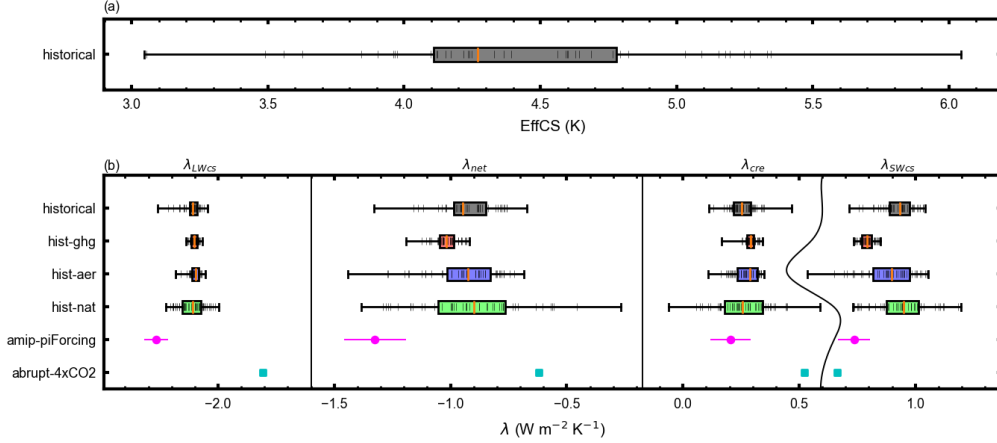


**Figure 3.** (a) Boxplot of EffCS across the historical ensemble (1850–2014). (b) Boxplots of feedbacks in the historical and single forcing ensembles (1850–2014), amip-piForcing experiment (1870–2014), and abrupt-4xCO2 experiment (first 150 years). For each boxplot, the vertical black lines indicate each ensemble member, the whiskers indicate the maximum and minimum feedbacks seen in the ensemble, the boxes indicate the interquartile range, and the vertical orange line represents the median value. Error bars on amip-piForcing indicate the 5–95% confidence interval, calculated from the standard error of the linear fit.

314 A further decomposition of  $\lambda_{cre}$  into shortwave and longwave components is shown  
 315 in Figure S1. There, the largest contribution to the spread in  $\lambda_{cre}$  comes from the short-  
 316 wave component, consistent with the strong influence of low cloud feedbacks, and the  
 317 cancelling of the longwave and shortwave response to changes in high cloud.

318 The feedbacks seen in each historical and single forcing experiment are largely con-  
 319 sistent with each other (i.e. differing forcing efficacies do not appear to be strongly ev-  
 320 ident in HadGEM3-GC3.1-LL), although a slightly more negative median feedback is seen  
 321 in the hist-ghg experiment, consistent with the findings of Salvi et al. (2022). In Figure  
 322 3, the more negative median feedback in the hist-ghg experiment is shown to be caused  
 323 by a weaker  $\lambda_{SWcs}$ , although due to the large spread in historical, hist-aer, and hist-nat  
 324 feedbacks, the lower tails of the feedbacks in these experiments extend to be more nega-  
 325 tive than the lower tail of the hist-ghg experiment. The amip-piForcing and abrupt-  
 326 4xCO2 feedbacks are also shown in Figure 3b. For each component of  $\lambda_{net}$ , the amip-  
 327 piForcing feedback lies towards the lower tail of the historical ensemble, a behaviour most  
 328 strongly seen in the  $\lambda_{SWcs}$ , and  $\lambda_{LWcs}$  components.

329 Maps of the ensemble mean feedbacks and amip-piForcing feedbacks are shown in  
 330 Figure 4 to help identify where different feedbacks are located and to highlight regions  
 331 where feedbacks differ across the range of experiments analysed. The spatial feedback  
 332 map is calculated by regressing the local  $(N-F)$  against the global mean  $T_s$  changes.  
 333 Here the ensemble mean feedbacks are calculated by taking the regression of the mean  
 334 rather than calculating the feedback for each ensemble member and averaging across the  
 335 ensemble. This was done to help reduce the noise in the regression of  $(N-F)$  and  $T_s$   
 336 when calculating the feedbacks.

337 From Figure 4, it can be seen that different feedbacks dominate in different regions.  
 338 For example, in general  $\lambda_{SWcs}$  is strongly positive at higher latitudes and small at lower  
 339 latitudes. This is because the sea ice feedback is a key feedback affecting the  $SW_{cs}$  fluxes.  
 340 The strong positive  $\lambda_{SWcs}$  seen over the northern hemisphere land masses is likely re-  
 341 lated to snow and land ice feedbacks, and the strong negative  $\lambda_{SWcs}$  seen in the South-  
 342 ern Ocean in the hist-aer experiment may be caused by ocean convective events that bring  
 343 warmer water to the surface due to destabilization of the ocean, similar to those discussed  
 344 in (Ridley et al., 2022).

345 With the exception of the Southern Ocean feature seen in the hist-aer experiment,  
 346 the  $\lambda_{LWcs}$  is generally negative everywhere across all experiments, although a few small  
 347 regions in the amip-piForcing experiment also have positive  $\lambda_{LWcs}$ . The  $\lambda_{LWcs}$  is largely  
 348 composed of the Planck, lapse rate, and water vapour feedbacks. This term is generally  
 349 large and negative due to the strong Planck response. Over the Southern Ocean in the  
 350 hist-aer experiment, since this region warms, which is of opposite sign to the cooling seen  
 351 over the rest of the planet, the  $\lambda_{LWcs}$  is strongly positive in this region. In the tropics,  
 352 the lapse rate and Planck feedbacks are typically negative, therefore the positive  $\lambda_{LWcs}$   
 353 regions in the amip-piForcing experiment over the tropics are likely caused by the wa-  
 354 ter vapour feedback (Stephens et al., 2016).

355  $\lambda_{cre}$  exhibits relatively large spatial variations. In the historical and single forcing  
 356 experiments (particularly hist-aer) a strongly positive  $\lambda_{cre}$  is seen over the North Pa-  
 357 cific, highlighting the role of positive cloud feedbacks in the sub-tropical cloud decks in  
 358 subsidence regions. Again,  $\lambda_{cre}$  has been decomposed into longwave and shortwave com-  
 359 ponents (Figure S2). The strong  $\lambda_{cre}$  over the North Pacific is caused by shortwave cloud  
 360 feedbacks, and over tropical high cloud regions, e.g. the Indo-Pacific warm pool region,  
 361 strong shortwave and longwave cloud feedbacks cancel, causing the relatively weak  $\lambda_{cre}$   
 362 over much of the tropics.

363 From these maps of feedbacks, it can be seen that although in the global mean, dif-  
 364 ferent efficacies are not particularly large in HadGEM3-GC3.1-LL, spatially, large vari-  
 365 ations do exist between the different experiments.

366 As mentioned in the introduction, differences in feedbacks across experiments and  
 367 ensemble members are generally thought to be fundamentally caused by differing SST  
 368 patterns. Therefore, to help understand the differences in feedbacks seen in Figure 4, en-  
 369 semble mean  $T_s$  patterns are shown in Figure 5. Similar to the maps of  $\lambda$ , these have been  
 370 calculated by regressing the ensemble mean local changes in  $T_s$  against the ensemble mean  
 371 global mean  $T_s$ , written as  $dT_s/d\bar{T}_s$ , where the bar indicates a global mean. In Figure  
 372 5, the strongest regions of  $dT_s/d\bar{T}_s$  occur in the Arctic, with weaker more spatially uni-  
 373 form  $dT_s/d\bar{T}_s$  seen over the tropics. Over the Southern Ocean, large variations in  $dT_s/d\bar{T}_s$   
 374 are seen across the different experiments. Here, hist-nat exhibits the strongest  $dT_s/d\bar{T}_s$   
 375 whilst hist-aer exhibits a negative  $dT_s/d\bar{T}_s$  (i.e. although global mean  $T_s$  is decreasing  
 376 in the hist-aer experiment, the southern ocean warms). As previously mentioned, this  
 377 may be caused by ocean convective events that bring warmer water to the surface due  
 378 to destabilization of the ocean (Ridley et al., 2022). In the northern hemisphere high lat-  
 379 itudes, hist-aer exhibits the strongest  $dT_s/d\bar{T}_s$ , possibly due to the aerosol  $F$  being pre-  
 380 dominantly based in the northern hemisphere. Over the tropics  $dT_s/d\bar{T}_s$  is relatively con-  
 381 sistent across each experiment.

382 Since one of the key aims of this paper is to understand the ensemble spread in feed-  
 383 backs, maps of the standard deviation in  $\lambda$  in the historical experiment help to highlight  
 384 the regions that contribute most to this spread (Figure 6). From Figure 6 it can be seen

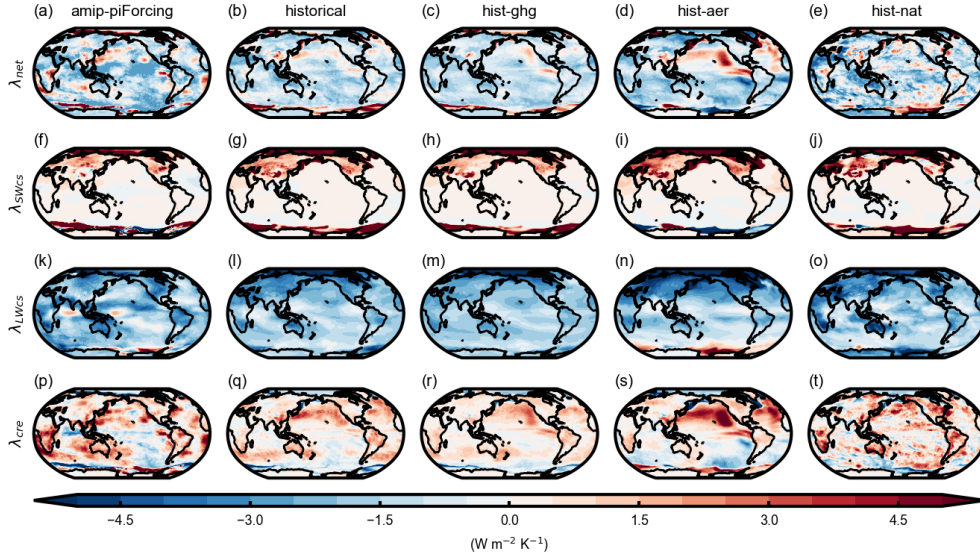


**Figure 4.** Maps of ensemble mean  $\lambda_{net}$ ,  $\lambda_{SWcs}$ ,  $\lambda_{LWcs}$ , and  $\lambda_{cre}$  in amip-piForcing, historical, hist-ghg, hist-aer, and hist-nat experiments. Here,  $\lambda$  has been calculated by regressing the ensemble mean local annual mean ( $N - F$ ) against the ensemble mean global annual mean  $T_s$  between 1850 – 2014 for historical and single forcing experiments, and 1870 – 2014 for amip-piForcing.

385 that for  $\lambda_{SWcs}$  most of the spread comes from the higher latitudes. In contrast, for  $\lambda_{cre}$ ,  
 386 variations in cloud feedbacks across the tropics and subtropics contribute to the spread.  
 387  $\lambda_{LWcs}$  exhibits the smallest standard deviations suggesting that this component contributes  
 388 less to the ensemble spread in feedbacks. This is likely due to the fact that the Planck,  
 389 lapse rate and water vapour feedbacks are highly constrained by model physics.

390 The three main scientific aims of this paper were to a) understand how natural variability  
 391 causes different feedbacks in response to the same imposed forcing (for example,  
 392 what is it that causes one historical ensemble member to have a net feedback of  $-1.3$   
 393  $\text{Wm}^{-2}\text{K}^{-1}$  whilst another has a feedback of  $-0.7 \text{Wm}^{-2}\text{K}^{-1}$ ?), b) understand what causes  
 394 different efficacies across different forcing agents, and c) investigate whether the AOGCM  
 395 historical simulations - where the model simulates its own SSTs - can capture the radiative  
 396 feedback and EffCS estimated from AGCM experiments prescribed with observed  
 397 SSTs (i.e. are the feedbacks seen in the historical experiment consistent with those seen  
 398 in amip-piForcing?). To address these questions, the different components of  $\lambda_{net}$  are  
 399 investigated in isolation, with Section 3.2 investigating  $\lambda_{SWcs}$ , Section 3.3 investigating  
 400  $\lambda_{LWcs}$ , and Section 3.4 investigating  $\lambda_{cre}$ .

### 401 3.2 Processes Affecting Shortwave Clear-sky Feedbacks ( $\lambda_{SWcs}$ )

402 This section aims to understand  $\lambda_{SWcs}$  in the historical and single forcing exper-  
 403 iments, addressing the cause of the ensemble spread, the disparity between historical and  
 404 amip-piForcing, and the cause of different efficacies across the different forcing agents.  
 405 Figure 3 shows that  $\lambda_{SWcs}$  is a key contributor to the ensemble spread in  $\lambda_{net}$ , and the  
 406 correlation between the two feedbacks is 0.82 across the historical experiment ensemble.  
 407 Both the maps of  $\lambda_{SWcs}$  and standard deviation in  $\lambda_{SWcs}$  (Figure 4 and Figure 6b) in-  
 408 dicate that most of the signal and spread in  $\lambda_{SWcs}$  comes from the higher latitudes, a  
 409 region where the sea ice albedo feedback is a key process. We suggest that this feedback

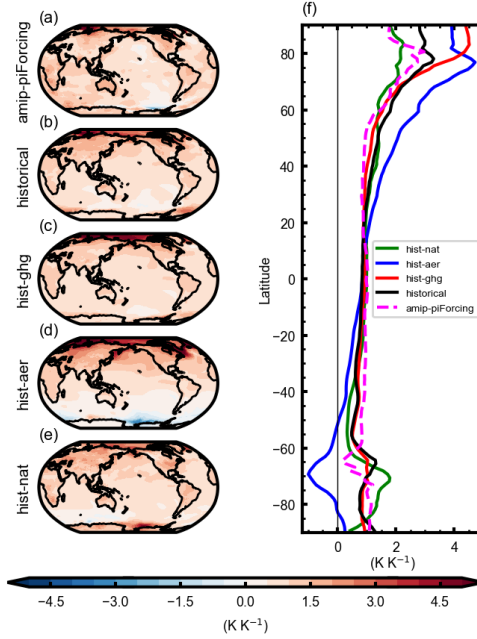


**Figure 5.** (left) maps of  $dT_s/d\bar{T}_s$  in  $\text{K K}^{-1}$  in each experiment; amip-piForcing, historical, hist-ghg, hist-aer, and hist-nat. Here,  $dT_s/d\bar{T}_s$  has been calculated by regressing the ensemble mean local annual mean  $T_s$  against the ensemble mean global annual mean  $T_s$  between 1850 – 2014 for historical and single forcing experiments, and 1870 – 2014 for amip-piForcing. (right) Zonal mean of maps to the left.

410 is a key contributor to the spread in  $\lambda_{SWCS}$  and a scatter plot of  $\lambda_{SWCS}$  against global  
 411 sea ice fraction change per degree of warming ( $d(\text{Sea Ice})/d\bar{T}_s$ ) shown in Figure 7a con-  
 412 firms this. There, a correlation of -0.84 is seen between the two variables in the histor-  
 413 ical experiment over the full time period from 1850 – 2014. As previously mentioned,  
 414 ultimately, the cause of differing feedbacks can be explained through variations in SST  
 415 patterns. To understand the varying  $d(\text{Sea Ice})/d\bar{T}_s$  and  $\lambda_{SWCS}$  across the ensemble, scatter  
 416 plots of polar  $dT_s/d\bar{T}_s$  against global  $d(\text{Sea Ice})/d\bar{T}_s$  and  $\lambda_{SWCS}$  are shown in Fig-  
 417 ure 7b and c respectively. Here polar  $dT_s/d\bar{T}_s$  is characterised by averaging over latitudes  
 418 greater than  $60^\circ\text{N}$  and lower than  $60^\circ\text{S}$ . From Figure 7b and c, a strong relationship be-  
 419 tween polar  $dT_s/d\bar{T}_s$  and both  $d(\text{Sea Ice})/d\bar{T}_s$  and  $\lambda_{SWCS}$  can be seen. This suggests that  
 420 the spread in  $\lambda_{SWCS}$  can be understood by the degree of polar amplification across the  
 421 ensemble.

422 Figure 7a also indicates that the sea ice albedo feedback is a key reason for the dif-  
 423 ferences in  $\lambda_{SWCS}$  between the historical and amip-piForcing experiments. Here, the amip-  
 424 piForcing experiment has been analysed only between 1980 and 2014 due to the unre-  
 425 alistic evolution of sea ice in the amip-piForcing experiment prior to 1980 when sea ice  
 426 observations were sparse (Titchner & Rayner, 2014; T. Andrews et al., 2018). It is there-  
 427 fore important to note that much of the absolute difference in  $\lambda_{SWCS}$  and  $d(\text{Sea Ice})/d\bar{T}_s$   
 428 between the amip-piForcing and historical experiments in Figure 7 may be due to the  
 429 different time frames analysed. The historical experiment has also been analysed between  
 430 1980 and 2014 (Figure 7 non-filled circles) and no substantial change in the relationship  
 431 between each variable is seen. This does not rule out the possibility that the amip-piForcing  
 432 evolution of sea ice, polar temperatures, and  $\lambda_{SWCS}$  may have been different for the longer

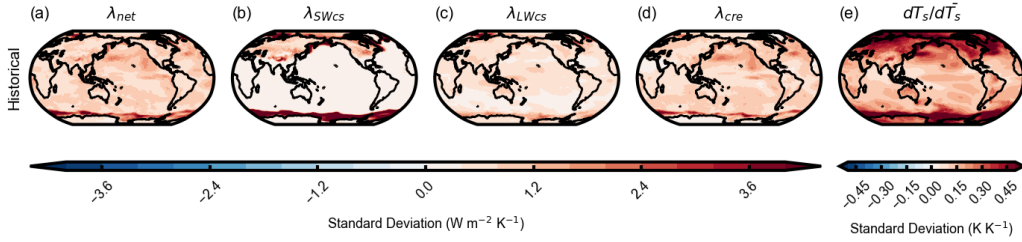


**Figure 6.** Maps of standard deviation in  $\lambda_{net}$ ,  $\lambda_{SWcs}$ ,  $\lambda_{LWcs}$ ,  $\lambda_{cre}$ , and  $dT_s/d\bar{T}_s$  in the historical experiment. Here,  $\lambda$  has been calculated by regressing the local changes in  $(N - F)$  against the global mean  $T_s$  change, and  $dT_s/d\bar{T}_s$  is the local  $T_s$  regressed against global mean  $T_s$ .

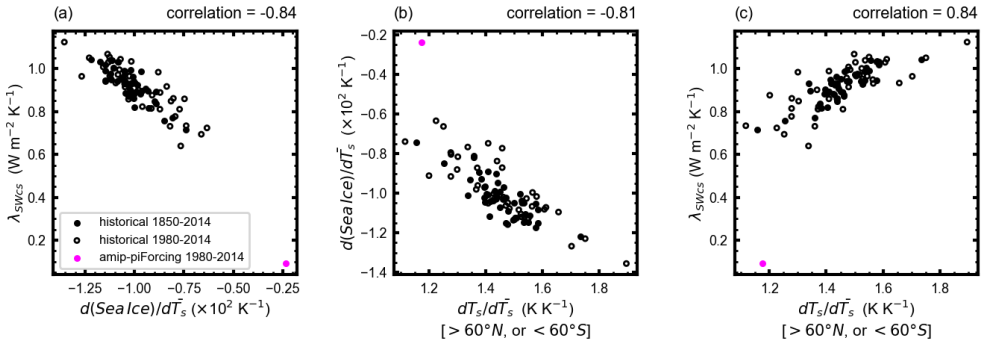


**Figure 7.** Scatter plots of (a) change in global sea ice per degree of warming against  $\lambda_{SWcs}$ , (b) change in  $T_s$  at latitudes greater than  $60^\circ\text{N}$  or lower than  $-60^\circ\text{S}$  per degree of global warming against change in global sea ice per degree of global warming, and (c) change in  $T_s$  at latitudes greater than  $60^\circ\text{N}$  or lower than  $60^\circ\text{S}$  per degree of global warming against  $\lambda_{SWcs}$ . Here, each black dot represents a historical ensemble member where values are calculated between 1850–2014 for the filled black dots, and 1980–2014 for the unfilled black dots. The magenta dots represent the amip-piForcing experiment calculated between 1980–2014 (due to sparse sea ice observations prior to 1980).

433 period, however, the fact that the amip-piForcing experiment is consistent with the re-  
 434 lationship seen in the historical experiment (demonstrated in Figure 7a) would suggest  
 435 that differences in  $\lambda_{SWcs}$  between historical and amip-piForcing experiments can be ex-  
 436 plained through this mechanism, and the smaller  $\lambda_{SWcs}$  in amip-piForcing is related to  
 437 the smaller  $d(\text{Sea Ice})/d\bar{T}_s$ . The fact that in 7b the amip-piForcing experiment does not  
 438 fit the historical ensemble relationship between polar  $dT_s/d\bar{T}_s$  and  $d(\text{Sea Ice})/d\bar{T}_s$  sug-  
 439 gests that that the AOGCMs simulation of the relationship between SSTs and sea ice  
 440 melt is not the same as the observed relationship in the real world (assuming the rela-  
 441 tionship seen in amip-piForcing is a good analogue for the real world).

442 Thus far the ensemble spread and the disparity between historical and amip-piForcing  
 443 estimates of  $\lambda_{SWcs}$  has been investigated. It is shown that the sea ice albedo feedback  
 444 is a key process responsible for both, with the level of arctic amplification providing the  
 445 link between ensemble spread in  $\lambda_{SWcs}$  and  $T_s$  patterns. Previously, Dessler (2020) also

446 investigated changes in sea ice and its impact on feedbacks. Consistent with the results  
 447 shown in Figure 7, Dessler (2020) also found sea ice variability to cause a large spread  
 448 in  $\lambda_{SWcs}$  in their historical ensemble with a different model, where these feedback vari-  
 449 ations were linked to changes in different modes of ocean variability. Since Figure 7 high-  
 450 lights a strong relationship between polar SSTs and sea ice, understanding causes of pol-  
 451 lar SST change and how they are predicted to evolve in a future climate is important.

452 Other processes could also contribute to the spread in  $\lambda_{SWcs}$ , such as snow melt.  
 453 This could be responsible for the strong  $\lambda_{SWcs}$  seen over the Northern Hemisphere land  
 454 masses in Figure 4 f, g, h, i, and j, and the spread in  $\lambda_{SWcs}$  seen in Figure 6b. However,  
 455 this process is not investigated further here since the strongest spread in  $\lambda_{SWcs}$  is seen  
 456 over the Arctic and Southern Oceans.

457 With the understanding gained from Figure 7, the different efficacies of each forc-  
 458 ing agent are investigated. Maps of ensemble mean  $\lambda_{SWcs}$  and  $dT_s/d\bar{T}_s$  are shown in Fig-  
 459 ure 8. Here, the hist-ghg experiment is shown and each of the other experiments are shown  
 460 relative to the hist-ghg values. This enables clearer identification of the differences be-  
 461 tween each forcing agent.

462 From Figure 8 the spatial pattern of  $dT_s/d\bar{T}_s$  and  $\lambda_{SWcs}$  are shown to be similar,  
 463 suggesting that the regional change in  $dT_s/d\bar{T}_s$  leads to regional changes in  $\lambda_{SWcs}$  due  
 464 to the close relationship between  $T_s$  and sea ice. This is true for both the northern and  
 465 southern hemisphere and also across each of the experiments. The spatial correlations  
 466 between  $dT_s/d\bar{T}_s$  and  $\lambda_{SWcs}$  across all experiments and each hemisphere are between  
 467 0.64 – 0.88, further highlighting the strong coupling between local  $T_s$  patterns and lo-  
 468 cal feedbacks. For the historical experiment, in the southern hemisphere, a stronger  $\lambda_{SWcs}$   
 469 is associated with a larger Southern Ocean  $dT_s/d\bar{T}_s$  relative to hist-ghg. The northern  
 470 hemisphere maps in 8b show contrasting feedbacks between the Arctic Ocean regions and  
 471 the slightly lower latitude regions around the Labrador Sea. Over the Arctic Ocean hist-  
 472 ghg has a stronger  $\lambda_{SWcs}$  compared to the historical simulations, whereas around the  
 473 Labrador Sea, the historical experiment has the stronger  $\lambda_{SWcs}$ . This is reflected in the  
 474  $dT_s/d\bar{T}_s$  patterns, where the historical experiment has a weaker  $dT_s/d\bar{T}_s$  over the Arc-  
 475 tic Ocean, but a stronger  $dT_s/d\bar{T}_s$  over the Labrador Sea. This northern hemisphere pat-  
 476 tern in  $\lambda_{SWcs}$  and  $dT_s/d\bar{T}_s$  relative to hist-ghg is similar to that seen in the hist-aer and  
 477 hist-nat experiment, where the hist-aer experiment demonstrates the largest positive  $\lambda_{SWcs}$   
 478 values and also extends these positive values furthest south.

479 In the southern hemisphere, unlike the historical experiment, the hist-aer exper-  
 480 iment shows strongly negative  $\lambda_{SWcs}$  and  $dT_s/d\bar{T}_s$  relative to the hist-ghg experiment.  
 481 As previously mentioned, this may be due to ocean convection in the Southern Ocean  
 482 triggered by the ocean becoming unstable (Ridley et al., 2022). This convection could  
 483 bring warmer water up from below, warming the surface, melting sea ice, and resulting  
 484 in a negative  $\lambda_{SWcs}$ .

485 Here, it has been shown that the sea ice albedo feedback and the level of arctic am-  
 486 plification is a key process in producing the large spread in  $\lambda_{SWcs}$  across the ensemble  
 487 and is also a key reason for the different feedback seen in the historical and amip-piForcing  
 488 experiments. It has also been shown that the different efficacies seen across the differ-  
 489 ent historical and single forcing experiments can be explained through differing SST pat-  
 490 terns (in agreement with Haugstad et al. (2017)), with the experiments with a stronger  
 491  $\lambda_{SWcs}$  locally, also exhibiting a larger  $dT_s/d\bar{T}_s$ .

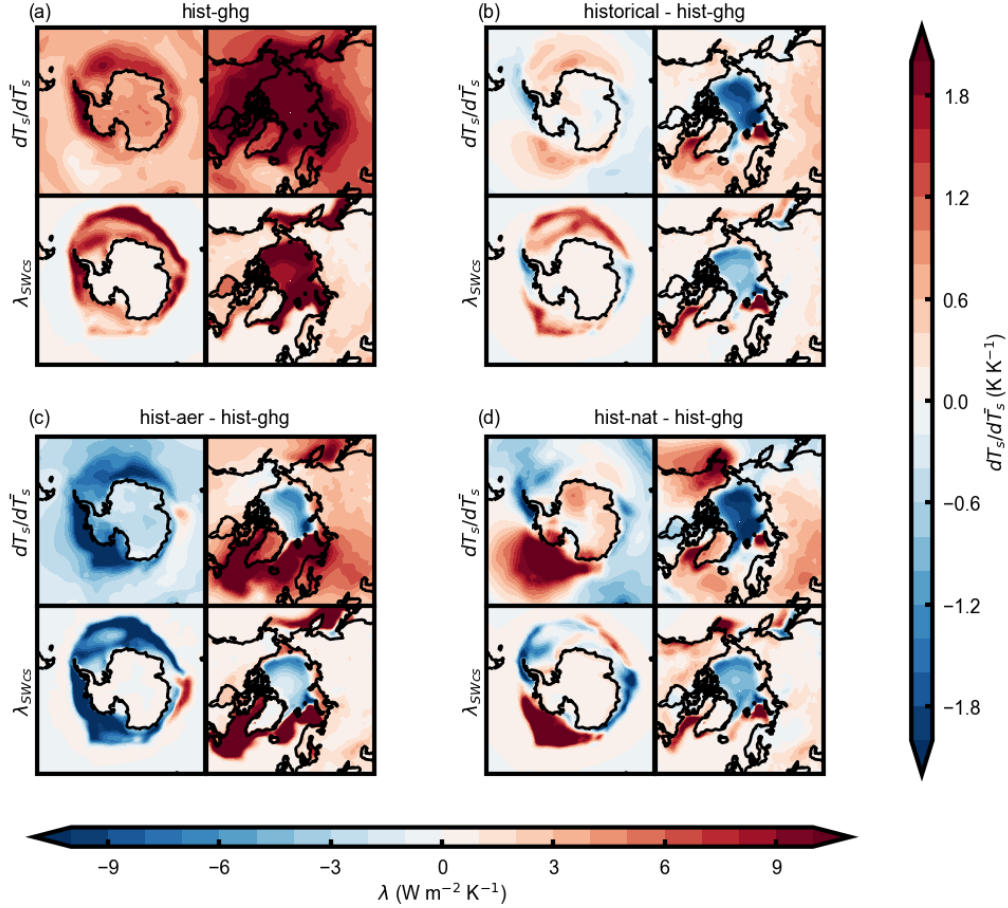


**Figure 8.** Maps of (top rows) surface warming pattern ( $\text{K K}^{-1}$ ) and (bottom rows)  $\lambda_{SWcs}$  over the (right columns) northern and (left columns) southern hemisphere poles in the (a) hist-ghg experiment and (b) historical, (c) hist-aer and (d) hist-nat experiments relative to hist-ghg.

492

### 3.3 Processes Affecting Longwave Clear-sky Feedbacks ( $\lambda_{LWcs}$ )

493

494

495

496

497

From Figure 3 it can be seen that whilst the  $\lambda_{LWcs}$  does not contribute much to the different efficacies seen in each of the historical and single forcing experiments, it does contribute to the spread in  $\lambda_{net}$  and is also a large source of disparity between the historical and amip-piForcing experiments. Understanding the spread in  $\lambda_{LWcs}$  and the disparity between the historical and amip-piForcing experiments is the aim of this section.

498

499

500

501

502

503

504

505

506

507

$\lambda_{LWcs}$  is determined by a combination of the Planck feedback, the water vapour feedback and the lapse rate feedback (T. Andrews & Webb, 2018). The water vapour and lapse rate feedbacks have been shown to be strongest in the tropical troposphere (Soden et al., 2008; T. Andrews & Webb, 2018), since the tropical atmosphere closely follows a moist adiabatic lapse rate and therefore any warming at the surface is amplified vertically in the atmosphere (Po-Chedley et al., 2018). To investigate the  $\lambda_{LWcs}$  in the historical ensemble, first, plots of zonal mean atmospheric temperature regressed against global mean  $T_s$  ( $dT_a/dT_s$ ) are analysed (Figure 9). Note that as previously discussed, here, the atmospheric temperature ( $T_a$ ) has had any changes associated with the forcing subtracted from it (see discussion following Equation 3). This means that the  $\text{CO}_2$

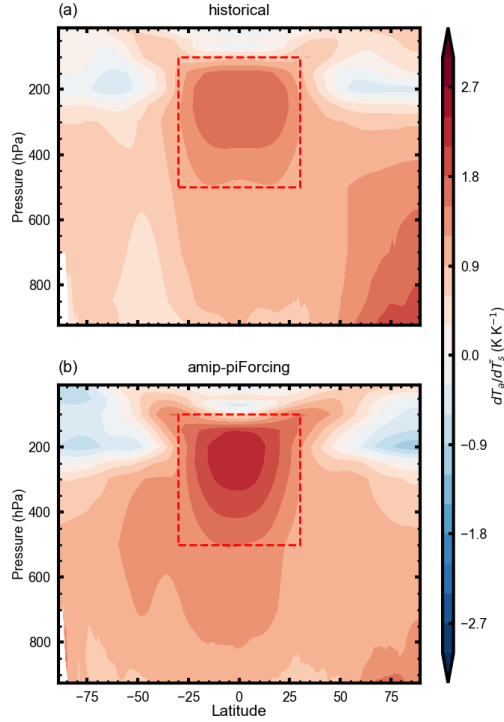


**Figure 9.** Zonal mean changes in temperature per degree of global warming in the (a) historical and (b) amip-piForcing experiments.

508 driven stratospheric cooling in the historical experiment is removed, and a more accu-  
 509 rate comparison between historical and amip-piForcing experiments can be made.

510 From Figure 9 the pattern of  $dT_a/d\bar{T}_s$  seen in both the historical and amip-piForcing  
 511 experiments demonstrates a marked warming over the tropical troposphere. Compar-  
 512 ing Figure 9b and c it can be seen that this tropospheric  $dT_a/d\bar{T}_s$  is stronger in amip-  
 513 piForcing compared to the historical experiment. The amip-piForcing experiment also  
 514 exhibits a stronger  $dT_a/d\bar{T}_s$  over the southern hemisphere troposphere, whilst the his-  
 515 torical experiment has a larger  $dT_a/d\bar{T}_s$  signal over the northern hemisphere high lat-  
 516 itudes. This is potentially due to the different  $T_s$  patterns seen in the historical and amip-  
 517 piForcing experiments, with the subtropical  $dT_s/d\bar{T}_s$  being slightly greater in the North-  
 518 ern Hemisphere in the historical ensemble and in the Southern Hemisphere in amip-piForcing  
 519 (Figure 5f).

520 Since the tropical troposphere is a key region in causing variations in  $\lambda_{LWcs}$ , a re-  
 521 gion between  $30^\circ\text{S} - 30^\circ\text{N}$  and between  $100 - 500$  hPa has been analysed further. A scat-  
 522 ter plot of tropical tropospheric  $dT_a/d\bar{T}_s$  against  $\lambda_{LWcs}$  is shown in Figure 10a. There  
 523 it can be seen that a strong correlation between the two variables exists with a corre-  
 524 lation coefficient of  $-0.8$ , consistent with physical expectations that a larger upper tro-  
 525 pical tropospheric temperature results in a larger lapse rate feedback and a more nega-  
 526 tive  $\lambda_{LWcs}$  (T. Andrews & Webb, 2018). The amip-piForcing tropical tropospheric  $dT_a/d\bar{T}_s$   
 527 and  $\lambda_{LWcs}$  has also been indicated in Figure 10a, where it can be seen that the tropi-  
 528 cal tropospheric  $dT_a/d\bar{T}_s$  does well to capture why the feedbacks in historical and amip-  
 529 piForcing experiments differ.

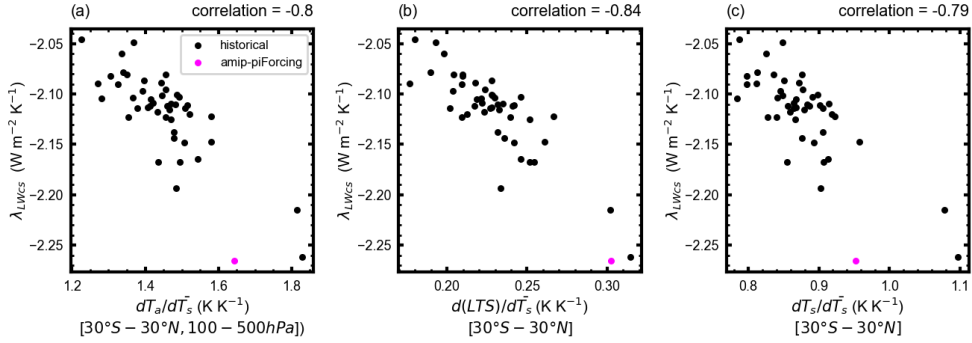


**Figure 10.** Scatter plots of (a) tropical tropospheric  $dT_a/d\bar{T}_s$  against  $\lambda_{LWcs}$ , (b) tropical Lower Tropospheric Stability (LTS) change per degree of global warming ( $d(LTS)/d\bar{T}_s$ ) against  $\lambda_{LWcs}$ , and (c) tropical  $dT_s/d\bar{T}_s$  against  $\lambda_{LWcs}$ . Here the tropics have been characterised by averaging between  $30^\circ\text{S}$  and  $30^\circ\text{N}$ , and the tropical troposphere has used the same latitudinal bounds and averaged between 100–500 hPa (see red boxes in Figure 9). In each plot, black dots represent the historical ensemble and amip-piForcing values are represented by a magenta dot.

530 Since the spread in feedbacks can ultimately be derived from differing SST patterns,  
 531 and given the strong relationship between tropical tropospheric temperature and  $\lambda_{LWcs}$ ,  
 532 the relationship between tropical mean  $dT_s/d\bar{T}_s$  and  $\lambda_{LWcs}$  has been investigated (Figure  
 533 10c). Figure 10c follows a similar analysis to that performed by Soden and Held (2006).  
 534 There, they demonstrated that across a range of models, due to the approximately adi-  
 535 abatic lapse rate of the tropical atmosphere, the strong coupling between the surface and  
 536 free troposphere in the tropics, and the relatively weak coupling present over higher lat-  
 537 itudes, the ratio between tropical and global warming was a good metric for determin-  
 538 ing the inter-model spread in lapse rate feedback. In Figure 10c it is shown that across  
 539 the historical ensemble, the tropical  $dT_s/d\bar{T}_s$  is well correlated with  $\lambda_{LWcs}$  with a cor-  
 540 relation coefficient of -0.79. It is clear that ensemble members with a stronger warming  
 541 over the tropics relative to the global mean also have a more strongly negative  $\lambda_{LWcs}$ .

542 As well as explaining the ensemble spread in  $\lambda_{LWcs}$ , tropical  $dT_s/d\bar{T}_s$  changes can  
 543 also be used to explain the disparity between amip-piForcing and historical experiments.  
 544 Figure 10c shows that the amip-piForcing experiment has a strong  $dT_s/d\bar{T}_s$  in the tropic-  
 545 s and also has a strong negative  $\lambda_{LWcs}$ .

### 546 3.4 Processes Affecting Cloud Feedbacks ( $\lambda_{cre}$ )

547 Although the historical ensemble used in this paper indicates that  $\lambda_{cre}$  is not the  
 548 feedback with the largest spread ( $\lambda_{SWcs}$  has a standard deviation of  $0.073 \text{ Wm}^{-2}\text{K}^{-1}$   
 549 whilst  $\lambda_{cre}$  has a standard deviation of  $0.06 \text{ Wm}^{-2}\text{K}^{-1}$ ), for long term estimates of Ef-  
 550 fCS across different models, cloud feedbacks are the largest source of uncertainty and  
 551 are the least understood (Forster et al., 2021; Ceppi & Nowack, 2021; Zelinka et al., 2016;  
 552 Ceppi et al., 2017). Because of this, over recent years, cloud feedbacks have been the fo-  
 553 cus of many studies. Cloud controlling factor analyses such as Ceppi and Nowack (2021)  
 554 and Blanco et al. (2023) aim to relate changes in clouds to other meteorological factors,  
 555 such as free tropospheric humidity (van der Dussen et al., 2015), SSTs (Bretherton &  
 556 Blossey, 2014), surface wind speed (Brueck et al., 2015) and inversion strength (Qu et  
 557 al., 2015; Klein et al., 2017; Kawai et al., 2017). By better understanding what factors

558 cause clouds to change, it is possible to understand differences in cloud feedbacks across  
559 models/ensembles.

560 In this section,  $\lambda_{cre}$  is investigated, primarily focusing on the spread across the his-  
561 torical experiment ensemble. Previously, Salvi et al. (2022) suggested that the different  
562 efficacies of well mixed greenhouse gases and aerosols were linked to changes in clouds  
563 due to differing changes in stability (although a large variability is seen across different  
564 models and a relatively small ensemble of 7 models was used). However here, the results  
565 shown in Figure 3 would suggest that for HadGEM3-GC3.1-LL,  $\lambda_{cre}$  does not contribute  
566 substantially to different forcing efficacies in the global mean. To understand the spa-  
567 tial distribution of  $\lambda_{cre}$ , Figure 4q is analysed. Here, strong positive cloud feedbacks are  
568 seen over the North Pacific and North Atlantic, and slightly weaker cloud feedbacks are  
569 seen over the Southern Indian Ocean and South Atlantic (each caused by positive short-  
570 wave cloud feedbacks - Figure S2). To understand the spread in  $\lambda_{cre}$ , maps of standard  
571 deviation in  $\lambda_{cre}$ ,  $\lambda_{SWcre}$ , and  $\lambda_{LWcre}$  and standard deviation in  $dT_s/d\bar{T}_s$  are shown in  
572 Figure 11. From Figure 11a it is possible to identify regions where the spread in  $\lambda_{cre}$  is  
573 largest and therefore which regions contribute most to the spread seen in Figure 3. The  
574 regions with the largest spread in  $\lambda_{cre}$  are the North Pacific and North Atlantic, due to  
575 a large spread in  $\lambda_{SWcre}$ . The Southern Ocean and low cloud deck regions off the east  
576 coast of South America, Australia and Southern Africa, also exhibit a moderately large  
577 standard deviation in  $\lambda_{cre}$ , again due to shortwave cloud feedbacks. The map of stan-  
578 dard deviation of  $\lambda_{LWcre}$  shows a large spread in feedbacks over the tropical ascent re-  
579 gions, however as previously discussed, in these regions, longwave and shortwave responses  
580 to changes in cloud cancel, and therefore the standard deviation in net cloud feedbacks  
581 in these regions is generally small.

582 The spatial distribution of the standard deviation in  $dT_s/d\bar{T}_s$  shown in Figure 11f  
583 is relatively similar to the pattern of standard deviation in  $\lambda_{cre}$ . Calculating the spatial  
584 correlation between Figures 11a and f, a correlation coefficient of 0.47 is found. Given  
585 surface temperatures are a key cloud controlling factor, as shown by Ceppi and Nowack  
586 (2021), we would expect the spread in  $\lambda_{cre}$  to be partly controlled by the spread in  $dT_s/d\bar{T}_s$ .

587 To better understand the cause of the spread in  $\lambda_{cre}$  shown in Figure 3b and 11a,  
588 two key cloud controlling factors are investigated; changes in  $T_s$  and changes in Lower  
589 Tropospheric Stability (LTS), both of which have strong statistical relationships with  
590 changes in clouds (Cutler et al., 2022; Klein & Hartmann, 1993; Ceppi & Nowack, 2021).  
591 Here LTS is defined as the 700hPa potential temperature minus the surface potential tem-  
592 perature (Cutler et al., 2022). Regarding the physical mechanisms of these relationships,  
593 LTS has been shown to influence cloud changes by controlling the amount of entrain-  
594 ment between the moist boundary layer and the drier free troposphere. The physical mech-  
595 anism whereby surface temperatures effect cloud changes is less well established. Webb  
596 et al. (2024) investigate a range of possible mechanism relating surface temperatures to  
597 changes in cloud, such as the impact of surface latent heat flux changes, vertical gradi-  
598 ents in humidity or moist static energy, or changes in downwelling longwave radiation  
599 caused by changing free tropospheric humidity. It was found that different mechanisms  
600 were plausible in some models and not in others. For HadGEM3-GC3.1-LL, only one sug-  
601 gested mechanism was not ruled out based on the models behaviour. This mechanism  
602 involved a reduction in low cloud due to a warming and a decrease in specific humidity  
603 due to an increase in upward longwave radiation from the surface (Ogura et al., 2023).

604 To relate changes in LTS and surface temperatures to changes in  $\lambda_{cre}$ , first two re-  
605 gions are investigated, the North West (NW) Pacific and North East (NE) Pacific (see  
606 Figure 11 boxes). These two regions were selected as being regions with a strong  $\lambda_{cre}$

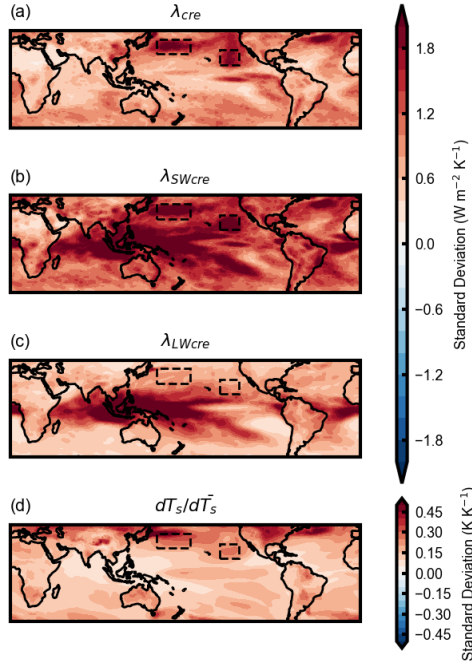


**Figure 11.** Maps of standard deviation in (a)  $\lambda_{cre}$ , (b)  $\lambda_{SWcre}$ , (c)  $\lambda_{LWcre}$ , and (d)  $dT_s/d\bar{T}_s$  across the historical ensemble. Dashed black boxes indicate regions analysed in Figure 12 with the NW Pacific region extending from 150–185°E and 26–41°N, and the NE Pacific region extending from 215–235°E and 15–30°N.

607 signal (Figure 4q) and spread (Figure 11a). The two regions also capture different cli-  
 608 matological regimes, with the NE Pacific a region of climatological subsidence where the  
 609 surface is decoupled from the free troposphere due to a strong inversion, whereas the NW  
 610 Pacific region is a region of climatological ascent where the surface is not decoupled from  
 611 the free troposphere. Scatter plots of  $d(LTS)/d\bar{T}_s$  and  $dT_s/d\bar{T}_s$  against  $\lambda_{cre}$  over the NW  
 612 Pacific and NE Pacific regions are shown in Figure 12a, b, c, and d. Here, it can be seen  
 613 that in both the NE and NW Pacific there is a strong correlation between  $dT_s/d\bar{T}_s$  and  
 614  $\lambda_{cre}$ , and  $d(LTS)/d\bar{T}_s$  and  $\lambda_{cre}$ . This is consistent with Ceppi and Nowack (2021). Al-  
 615 though the amip-piForcing and historical estimates of  $\lambda_{cre}$  were not particularly differ-  
 616 ent, for completeness, amip-piForcing values have also been indicated in Figure 12. Here  
 617 it can be seen that the amip-piForcing values fit the historical relationship between  $\lambda_{cre}$   
 618 and both  $dT_s/d\bar{T}_s$  and  $d(LTS)/d\bar{T}_s$  suggesting that any differences in  $\lambda_{cre}$  between his-  
 619 torical and amip-piForcing experiments in these regions can be explained through these  
 620 cloud controlling factors.

621 Since the LTS is defined as the 700hPa potential temperature minus the surface  
 622 potential temperature, it is possible that the strong correlations between  $d(LTS)/d\bar{T}_s$   
 623 and  $\lambda_{cre}$  exist primarily because of the strong relationship between  $\lambda_{cre}$  and  $dT_s/d\bar{T}_s$ .  
 624 To investigate this, scatter plots of 700hPa  $dT_a/d\bar{T}_s$  against  $\lambda_{cre}$  are shown in Figure 12e  
 625 and f. Here, differing relationships between the two variables exist over the two regions  
 626 analysed. Over the NW Pacific, a strong correlation remains with a correlation coeffi-  
 627 cient of 0.84. Over the NE Pacific however, this is not the case and a weak correlation

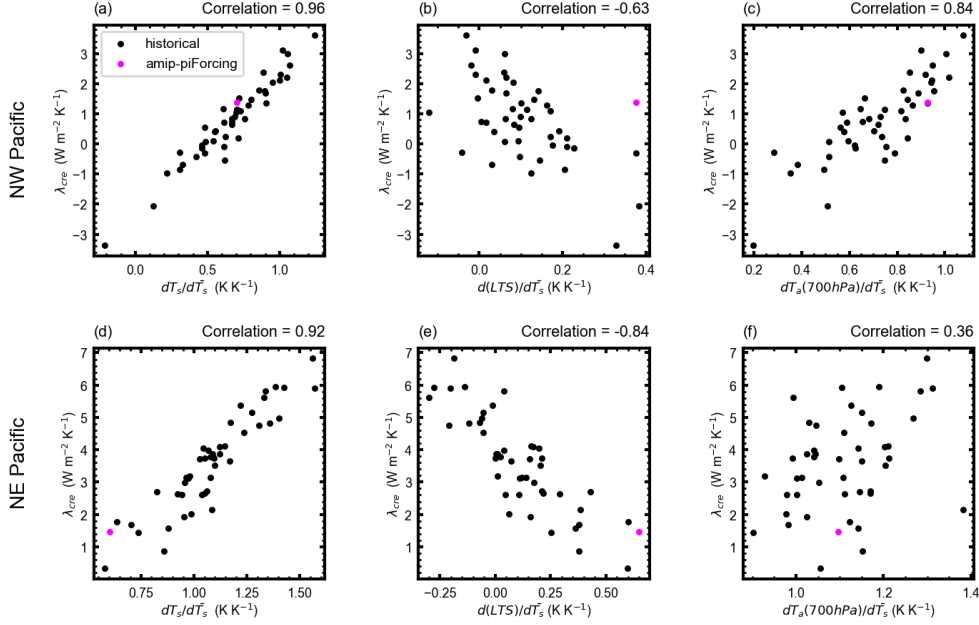


**Figure 12.** Scatter plots of (a and b)  $dT_s/d\bar{T}_s$ , (c and d)  $d(LTS)/d\bar{T}_s$ , and (e and f) 700hPa  $dT_a/d\bar{T}_s$  against  $\lambda_{cre}$  over the (a, c, and e) NW Pacific region, and (b, d, and f) NE Pacific region. Black dots represent the historical ensemble and magenta markers indicate amip-piForcing values.

628 of 0.36 is seen. This differing relationship may be due to the different convective regimes  
 629 that exist over the two regions. Over the NE Pacific, the strong inversion and the de-  
 630 coupling between the boundary layer and the free troposphere means that any surface  
 631 warming in this region will be trapped under the strong inversion. Over the NW Pacific,  
 632 this is not the case and surface warming can be transported efficiently into the free tro-  
 633 posphere. Therefore, to some degree, over the NW Pacific the 700hPa temperature is still  
 634 controlled by the temperatures at the surface.

635 An alternative approach is taken in Figure 13. Here, the local effect of surface warm-  
 636 ing and the remote effect of large scale stability changes on  $\lambda_{cre}$  is investigated using maps  
 637 of the correlation across the historical ensemble between local  $\lambda_{cre}$  and either the local  
 638  $dT_s/d\bar{T}_s$  or the 50°S – 50°N mean 700hPa  $dT_a/d\bar{T}_s$ . These latitudinal bounds were pre-  
 639 viously used by Ceppi and Gregory (2019) and Salvi et al. (2023) to capture large scale  
 640 tropospheric stability.

641 From Figure 13 it can be seen that generally, the local  $dT_s/d\bar{T}_s$  is the most strongly  
 642 correlated, with many regions exhibiting correlations greater than 0.7. The correlations  
 643 between  $\lambda_{cre}$  and the 50°S – 50°N mean 700hPa  $dT_a/d\bar{T}_s$  tend to be weaker, although  
 644 the subtropical cloud deck regions over the East Pacific and the Indian Ocean do exhibit  
 645 positive correlations (note these are not statistically significant at the 95% confidence  
 646 range). A decomposition of Figure 13 into shortwave and longwave components is shown  
 647 in Figure S3. Here the strong correlations seen in the low cloud deck regions in Figure  
 648 13 are associated with the shortwave cloud feedbacks, and similar to Figure 11 and S2,  
 649 the tropical ascent regions exhibit relatively strong correlations with both local  $dT_s/d\bar{T}_s$   
 650 and 50°S – 50°N mean 700hPa  $dT_a/d\bar{T}_s$  in the shortwave and longwave, however these

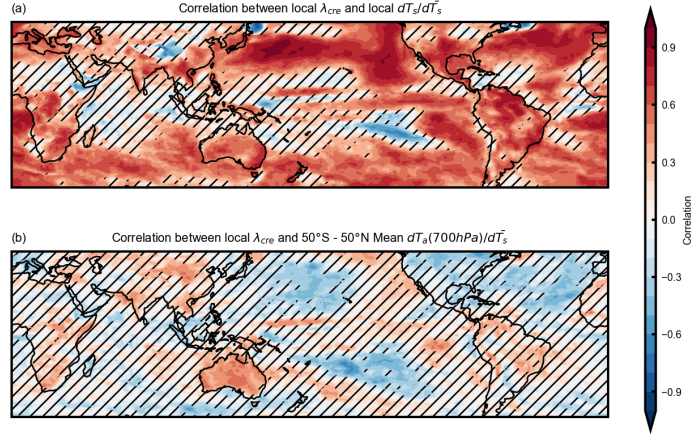


**Figure 13.** Maps of correlation between local  $\lambda_{cre}$  against (a) local  $dT_s/d\bar{T}_s$ , and (b) 50°S – 50°N mean 700hPa  $dT_a/d\bar{T}_s$  across the historical ensemble. Hatching indicates where correlations are not significant at the 95% confidence interval (i.e. p values are greater than 0.05). Here the p value approximately indicates the probability of two random distributions producing a correlation coefficient at least as great as those indicated in the colored contours.

651 two components cancel, resulting in the net cloud feedback correlation being relatively  
652 weak in those regions in Figure 13.

653 To summarise, cloud feedbacks are the largest source of uncertainty in EffCS across  
654 models, however within the HadGEM3-GC3.1-LL historical ensemble,  $\lambda_{SWCS}$  contributes  
655 more to the spread in  $\lambda_{net}$ . Spread in  $\lambda_{cre}$  can be explained through the cloud control-  
656 ling factors of  $T_s$  and LTS where  $dT_s/d\bar{T}_s$  is positively correlated with  $\lambda_{cre}$  and  $d(LTS)/d\bar{T}_s$   
657 is negatively correlated with  $\lambda_{cre}$ . Finally, it is shown that the local influence of  $dT_s/d\bar{T}_s$   
658 on  $\lambda_{cre}$  is much stronger than the remote effect of changes in large scale atmospheric sta-  
659 bility.

#### 660 4 Conclusion

661 In this paper the feedbacks across a 47 member ensemble of historical and single  
662 forcing simulations have been analysed. Across the historical ensemble, EffCS ranges be-  
663 tween 3–6K, highlighting the large spread in estimated feedbacks caused by internal vari-  
664 ability. The aims of this work have been to understand the main causes of this spread  
665 in feedbacks across the ensemble, to understand if and why different forcing agents have  
666 different forcing efficacies, and finally to understand why the coupled historical simula-  
667 tions struggle to capture the feedbacks seen in AGCM simulations forced by observed  
668 SSTs. To address these aims, three components of  $\lambda_{net}$  were investigated ( $\lambda_{SWCS}$ ,  $\lambda_{LWCS}$ ,  
669 and  $\lambda_{cre}$ ).

670 The analysis found that the ensemble spread in  $\lambda_{SWCS}$  is largely caused by vary-  
671 ing degrees of sea ice melt per degree of global warming. Ensemble members that showed  
672 a large reduction in sea ice per degree of global warming also exhibited a strong  $\lambda_{SWCS}$ ,  
673 with a correlation of -0.84 (consistent with Dessler (2020)). It was shown that this re-  
674 lationship was due to varying SST patterns, with ensemble members simulating stronger

675 polar amplification also exhibiting more sea ice melt and a stronger  $\lambda_{SWcs}$  (with a cor-  
 676 relation of 0.84 between polar SSTs and  $\lambda_{SWcs}$ ). This relationship between  $\lambda_{SWcs}$ , sea  
 677 ice melt, and polar amplification is also shown to be the reason for a much weaker  $\lambda_{SWcs}$   
 678 in the amip-piForcing experiment. Here, weaker polar amplification resulted in less sea  
 679 ice melt per degree of global warming and a smaller  $\lambda_{SWcs}$ . Finally, the different  $\lambda_{SWcs}$   
 680 between the different single forcing experiments was investigated, since  $\lambda_{SWcs}$  was found  
 681 to be the biggest source of differing forcing efficacies across the different forcing agents.  
 682 It was shown that different patterns of surface warming were the main cause of differ-  
 683 ent feedbacks across each experiment, with spatial correlations of 0.64 – 0.88 between  
 684 patterns of  $T_s$  change per degree of global warming and  $\lambda_{SWcs}$  across all experiments  
 685 and each hemisphere.

686 Previously, Salvi et al. (2022) also investigated different forcing efficacies between  
 687 different forcing agents, also finding the hist-aer experiment to exhibit more strongly am-  
 688 plifying feedbacks compared to hist-ghg. There they focused on influence of stability changes  
 689 on changes in cloud feedbacks, however here, we find that for HadGEM3-GC3.1-LL, changes  
 690 in sea ice and polar  $T_s$  play a larger role in causing different forcing efficacies.

691 The ensemble spread in  $\lambda_{LWcs}$  was also investigated. Here it was shown that both  
 692 tropical tropospheric temperature changes per degree of global warming and tropical  $T_s$   
 693 changes per degree of global warming were a key factor in causing the spread in  $\lambda_{LWcs}$ .  
 694 Here, increased tropical surface warming caused warming in the tropical troposphere which  
 695 has previously been shown to cause a stronger lapse rate feedback (T. Andrews & Webb,  
 696 2018). This relationship between  $\lambda_{LWcs}$  and tropical  $T_s$  also captures why the  $\lambda_{LWcs}$   
 697 is much stronger in the amip-piForcing experiment compared to the historical simula-  
 698 tions, with the amip-piForcing experiment exhibiting a stronger tropical surface warm-  
 699 ing per degree of global warming compared to most historical ensemble members. Given  
 700 that the amip-piForcing experiment is prescribed with observed SSTs, this shows how  
 701 AOGCM biases in tropical SST patterns can impact on the estimated  $\lambda_{LWcs}$ .

702 The final feedback to be investigated was  $\lambda_{cre}$ . In contrast to the primary role of  
 703  $\lambda_{cre}$  in causing uncertainty in long term estimates of climate sensitivity, in the HadGEM3-  
 704 GC3.1-LL historical ensemble, other feedbacks have a larger spread. Investigating  $\lambda_{cre}$ ,  
 705 it was shown that both  $T_s$  and LTS are key factors affecting changes in cloud feedbacks.  
 706 It is also shown that although amip-piForcing and historical cloud feedbacks are not too  
 707 dissimilar, both the LTS and  $T_s$  are useful metrics for understanding how amip-piForcing  
 708 cloud feedbacks relate to those seen in the historical simulations. The analysis concludes  
 709 by investigating the relative importance of local effect of varying  $T_s$  or the remote effect  
 710 of large scale changes in atmospheric stability. Here it is shown that the local  $T_s$  is the  
 711 most important, whilst the large scale stability plays a non-negligible role over the sub-  
 712 tropical cloud deck regions.

713 This work provides useful insight into the different feedbacks seen across different  
 714 forcing experiments and also provides information as to why coupled historical simula-  
 715 tions struggle to capture the feedbacks seen in the amip-piForcing experiment. To take  
 716 this work further, this large ensemble could be used to better understand the temporal  
 717 evolution of feedbacks. In recent years, the amip-piForcing experiment demonstrates a  
 718 marked decrease in  $\lambda_{net}$  (T. Andrews et al., 2022), and this ensemble could be used to  
 719 investigate whether a similar behaviour is captured in any of the ensemble members. This  
 720 work could then be used shed light on the causes and mechanisms involved in transient  
 721 feedbacks.

## 5 Open Research

Data used in this analysis consists of HadGEM3-GC3.1-LL model simulations performed as part of the Met Office’s contribution to CMIP6 (Eyring et al., 2016) and LESFMIP (D. Smith et al., 2022) and can be accessed from the ESGF CEDA data node <https://esgf-index1.ceda.ac.uk/search/cmip6-ceda/>.

### Acknowledgments

All authors were supported by the Met Office Hadley Centre Climate Programme funded by DSIT. Doug Smith was also supported by the European Commission Horizon 2020 CONSTRAIN project.

### References

- Adams, B. K., & Dessler, A. E. (2019). Estimating transient climate response in a large-ensemble global climate model simulation. *Geophysical Research Letters*, *46*, 311–317. doi: 10.1029/2018GL080714
- Andrews, M. B., Ridley, J. K., Wood, R. A., Andrews, T., Blockley, E. W., Booth, B., ... Sutton, R. T. (2020). Historical simulations with hadgem3-gc3.1 for cmip6. *Journal of Advances in Modeling Earth Systems*, *12*. doi: 10.1029/2019MS001995
- Andrews, T., Andrews, M. B., Bodas-Salcedo, A., Jones, G. S., Kuhlbrodt, T., Manners, J., ... Tang, Y. (2019). Forcings, feedbacks and climate sensitivity in hadgem3-gc3.1 and ukesm1. *Journal of Advances in Modeling Earth Systems*, *11*, 4377–4394. doi: 10.1029/2019MS001866
- Andrews, T., Bodas-Salcedo, A., Gregory, J. M., Dong, Y., and D. Paynter, K. C. A., Lin, P., ... Liu, C. (2022). On the effect of historical sst patterns on radiative feedback. *Journal of Geophysical Research: Atmospheres*, *127*. doi: 10.1029/2022JD036675
- Andrews, T., Gregory, J. M., Paynter, D., Silvers, L. G., Zhou, C., Mauritsen, T., ... Titchner, H. (2018). Accounting for changing temperature patterns increases historical estimates of climate sensitivity. *Geophysical Research Letters*, *45*, 8490–8499. doi: 10.1029/2018GL078887
- Andrews, T., Gregory, J. M., & Webb, M. J. (2015). The dependence of radiative forcing and feedback on evolving patterns of surface temperature change in climate models. *Journal of Climate*, *28*, 1630–1648. doi: 10.1175/JCLI-D-14-00545.1
- Andrews, T., Gregory, J. M., Webb, M. J., & Taylor, K. E. (2012). Forcings, feedbacks and climate sensitivity in cmip5 coupled atmosphere-ocean climate models. *Geophysical Research Letters*, *39*. doi: 10.1029/2012GL051607
- Andrews, T., & Webb, M. J. (2018). The dependence of global cloud and lapse rate feedbacks on the spatial structure of tropical pacific warming. *Journal of Climate*, *31*, 641–654. doi: 10.1175/JCLI-D-17-0087.1
- Blanco, J. E., Caballero, R., Datsleris, G., Stevens, B., Bony, S., Hadas, O., & Kaspi, Y. (2023). A cloud-controlling factor perspective on the hemispheric asymmetry of extratropical cloud albedo. *Journal of Climate*, *36*, 1793–1804. doi: 10.1175/JCLI-D-22-0410.1
- Bretherton, C. S., & Blossey, P. N. (2014). Low cloud reduction in a greenhouse-warmed climate: Results from lagrangian les of a subtropical marine cloudiness transition. *Journal of Advances in Modeling Earth Systems*, *6*, 91–114. doi: 10.1002/2013MS000250
- Brueck, M., Nuijens, L., & Stevens, B. (2015). On the seasonal and synoptic time-scale variability of the north atlantic trade wind region and its low-level clouds. *Journal of the Atmospheric Sciences*, *72*, 1428–1446. doi: 10.1175/JAS-D-14-0054.1

- 773 Ceppi, P., Brient, F., Zelinka, M. D., & Hartmann, D. L. (2017). Cloud feedback  
774 mechanisms and their representation in global climate models. *WIREs Climate*  
775 *Change*, 8. doi: 10.1002/wcc.465
- 776 Ceppi, P., & Gregory, J. M. (2019). A refined model for the earth’s global energy  
777 balance. *Climate Dynamics*, 53, 4781–4797. doi: 10.1007/s00382-019-04825-x
- 778 Ceppi, P., & Nowack, P. (2021). Observational evidence that cloud feedback ampli-  
779 fies global warming. *PNAS*, 118. doi: 10.1073/pnas.2026290118
- 780 Cutler, L., Brunke, M. A., & Zeng, X. (2022). Re-evaluation of low cloud amount re-  
781 lationships with lower-tropospheric stability and estimated inversion strength.  
782 *Geophysical Research Letters*, 49. doi: 10.1029/2022GL098137
- 783 Dessler, A. E. (2020). Potential problems measuring climate sensitivity from the his-  
784 torical record. *Journal of Climate*, 33, 2237–2248. doi: 10.1175/JCLI-D-19-  
785 -0476.1
- 786 Dessler, A. E., Mauritsen, T., & Stevens, B. (2018). The influence of internal vari-  
787 ability on earth’s energy balance framework and implications for estimating  
788 climate sensitivity. *Atmospheric Chemistry and Physics*, 18, 5147–5155. doi:  
789 10.5194/acp-18-5147-2018
- 790 Dong, Y., Armour, K. C., Proistosescu, C., Andrews, T., Battisti, D. S., Forster,  
791 P. M., ... Shiogama, H. (2021). Biased estimates of equilibrium climate sensi-  
792 tivity and transient climate response derived from historical cmip6 simulations.  
793 *Geophysical Research Letters*, 48. doi: 10.1029/2021GL095778
- 794 Eyring, V., Bony, S., Meehl, G. A., Senior, C. A., Stevens, B., Stouffer, R. J., &  
795 Taylor, K. E. (2016). Overview of the coupled model intercomparison project  
796 phase 6 (cmip6) experimental design and organization. *Geoscientific Model*  
797 *Development*, 9, 1937–1958. doi: 10.5194/gmd-9-1937-2016
- 798 Forster, P. M., Richardson, T., Maycock, A. C., Smith, C. J., Samset, B. H., Myhre,  
799 G., ... Schulz, M. (2016). Recommendations for diagnosing effective radiative  
800 forcing from climate models for cmip6. *Journal of Geophysical Research:*  
801 *Atmospheres*, 121, 12,460–12,475. doi: 10.1002/2016JD025320
- 802 Forster, P. M., Storelvmo, T., Armour, K., Collins, W., Dufresne, J.-L., Frame,  
803 D., ... co authors (2021). The earth’s energy budget, climate feed- backs,  
804 and climate sensitivity. In *Climate change 2021: The physical science basis.*  
805 *contribution of working group i to the sixth assessment report of the intergov-*  
806 *ernmental panel on climate change* (p. 93). Cambridge, UK and New York,  
807 USA: Cambridge University Press.
- 808 Fueglistaler, S., & Silvers, L. G. (2021). The peculiar trajectory of global  
809 warming. *Journal of Geophysical Research: Atmospheres*, 126. doi:  
810 10.1029/2020JD033629
- 811 Gillett, N. P., Shiogama, H., Funke, B., Hegerl, G., Knutti, R., Matthes, K., ...  
812 Tebaldi, C. (2016). The detection and attribution model intercomparison  
813 project (damip v1.0) contribution to cmip6. *Geoscientific Model Development*,  
814 9, 3685–3697. doi: 10.5194/gmd-9-3685-2016
- 815 Gregory, J. M., & Andrews, T. (2016). Variation in climate sensitivity and feedback  
816 parameters during the historical period. *Geophysical Research Letters*, 43,  
817 3911–3920. doi: 10.1002/2016GL068406
- 818 Gregory, J. M., Andrews, T., Ceppi, P., Mauritsen, T., & Webb, M. J. (2020).  
819 How accurately can the climate sensitivity to co2 be estimated from his-  
820 torical climate change? *Climate Dynamics*, 54, 129–157. doi: 10.1007/  
821 s00382-019-04991-y
- 822 Gregory, J. M., Ingram, W. J., Palmer, M. A., Jones, G. S., Stott, P. A., Thorpe,  
823 R. B., ... Williams, K. D. (2004). A new method for diagnosing radiative  
824 forcing and climate sensitivity. *Geophysical Research Letters*, 31. doi:  
825 10.1029/2003GL018747
- 826 Hansen, J., Sato, M., Ruedy, R., Nazarenko, L., Lacis, A., Schmidt, G. A., ...  
827 Zhang, S. (2005). Efficacy of climate forcings. *Journal of Geophysical Re-*

- 828 *search: Atmospheres, 110*. doi: 10.1029/2005JD005776
- 829 Haugstad, A. D., Armour, K. C., Battisti, D. S., & Rose, B. E. J. (2017). Relative  
830 roles of surface temperature and climate forcing patterns in the inconstancy  
831 of radiative feedbacks. *Geophysical Research Letters, 44*, 7455–7463. doi:  
832 10.1002/2017GL074372
- 833 Hwang, Y.-T., Xie, S.-P., Chen, P.-J., Tseng, H.-Y., & Deser, C. (2024). Contri-  
834 bution of anthropogenic aerosols to persistent la niña-like conditions in the  
835 early 21st century. *Proceedings of the National Academy of Sciences, 121*. doi:  
836 10.1073/pnas.2315124121
- 837 Kawai, H., Koshiro, T., & Webb, M. J. (2017). Interpretation of factors controlling  
838 low cloud cover and low cloud feedback using a unified predictive index. *Jour-  
839 nal of Climate, 30*, 9119–9131. doi: 10.1175/JCLI-D-16-0825.1
- 840 Kay, J. E., Deser, C., Phillips, A., Mai, A., Hannay, C., Strand, G., ... Verten-  
841 stein, M. (2015). The community earth system model (cesm) large ensemble  
842 project. *Bulletin of the American Meteorological Society, 1333–1349*. doi:  
843 10.1175/BAMS-D-13-00255.1
- 844 Kay, J. E., Holland, M. M., & Jahn, A. (2011). Inter-annual to multi-decadal arctic  
845 sea ice extent trends in a warming world. *Geophysical Research Letters, 38*.  
846 doi: 10.1029/2011GL048008
- 847 Klein, S. A., Hall, A., Norris, J. R., & Pincus, R. (2017). Low-cloud feedbacks from  
848 cloud-controlling factors: A review. *Surveys in Geophysics, 38*, 1307–1329. doi:  
849 10.1007/s10712-017-9433-3
- 850 Klein, S. A., & Hartmann, D. L. (1993). The seasonal cycle of low stratiform clouds.  
851 *Journal of Climate, 6*, 1587–1606. doi: 10.1175/1520-0442(1993)006<1587:  
852 TSCOLS>2.0.CO;2
- 853 Lambert, F. H., Webb, M. J., & Joshi, M. M. (2011). The relationship between  
854 land–ocean surface temperature contrast and radiative forcing. *Journal of Cli-  
855 mate, 24*, 3239 - 3256. doi: 10.1175/2011JCLI3893.1
- 856 Marvel, K., Schmidt, G. A., Miller, R. L., & Nazarenko, L. S. (2015). Implications  
857 for climate sensitivity from the response to individual forcings. *Nature Climate  
858 Change, 6*, 386–389. doi: 10.1038/NCLIMATE2888
- 859 Ogura, T., Webb, M. J., & Lock, A. P. (2023). Positive low cloud feedback  
860 primarily caused by increasing longwave radiation from the sea surface in  
861 two versions of a climate model. *Geophysical Research Letters, 50*. doi:  
862 10.1029/2023GL104786
- 863 Pincus, R., Forster, P. M., & Stevens, B. (2016). The radiative forcing model in-  
864 tercomparison project (rfmip): experimental protocol for cmip6. *Geoscientific  
865 Model Development, 9*, 3447–3460. doi: 10.5194/gmd-9-3447-2016
- 866 Po-Chedley, S., Armour, K. C., Bitz, C. M., Zelinka, M. D., Santer, B. D., & Fu, Q.  
867 (2018). Sources of intermodel spread in the lapse rate and water vapor feed-  
868 backs. *Journal of Climate, 31*, 3187 - 3206. doi: 10.1175/JCLI-D-17-0674.1
- 869 Proistosescu, C., & Huybers, P. J. (2017). Slow climate mode reconciles historical  
870 and model-based estimates of climate sensitivity. *Science Advances, 3*. doi: 10  
871 .1126/sciadv.1602821
- 872 Qu, X., Hall, A., Klein, S. A., & DeAngelis, A. M. (2015). Positive tropical ma-  
873 rine low-cloud cover feedback inferred from cloud-controlling factors. *Geophys-  
874 ical Research Letters, 42*, 7767–7775. doi: 10.1002/2015GL065627
- 875 Richardson, T. B., Forster, P. M., Smith, C. J., Maycock, A. C., Wood, T., An-  
876 drews, T., ... Watson-Parris, D. (2019). Efficacy of climate forcings in pdrmip  
877 models. *Journal of Geophysical Research: Atmospheres, 124*, 12824–12844. doi:  
878 10.1029/2019JD030581
- 879 Ridley, J. K., Blockley, E. W., & Jones, G. S. (2022). A change in climate state  
880 during a pre-industrial simulation of the cmip6 model hadgem3 driven by deep  
881 ocean drift. *Geophysical Research Letters, 49*. doi: 10.1029/2021GL097171
- 882 Rugenstein, M., & Armour, K. C. (2021). Three flavours of radiative feedbacks

- 883 and their implications for estimating equilibrium climate sensitivity. *Geophysical*  
 884 *Research Letters*, *48*. doi: 10.1029/2021GL092983
- 885 Rugenstein, M., Bloch-Johnson, J., Abe-Ouchi, A., Andrews, T., Beyerle, U., Cao,  
 886 L., ... Yang, S. (2019). Longrunmip: Motivation and design for a large  
 887 collection of millennial-length aogcm simulations. *Bulletin of the American*  
 888 *Meteorological Society*, *100*, 2551–2570. doi: 10.1175/BAMS-D-19-0068.1
- 889 Salvi, P., Ceppi, P., & Gregory, J. M. (2022). Interpreting differences in radiative  
 890 feedbacks from aerosols versus greenhouse gases. *Geophysical Research Letters*,  
 891 *49*. doi: 10.1029/2022GL097766
- 892 Salvi, P., Gregory, J. M., & Ceppi, P. (2023). Time-evolving radiative feedbacks in  
 893 the historical period. *Journal of Geophysical Research: Atmospheres*, *128*. doi:  
 894 10.1029/2023JD038984
- 895 Sherwood, S. C., Webb, M. J., Annan, J. D., Armour, K. C., Forster, P. M., Har-  
 896 greaves, J. C., ... Zelinka, M. D. (2020). An assessment of earth’s climate  
 897 sensitivity using multiple lines of evidence. *Reviews of Geophysics*, *58*(4). doi:  
 898 10.1029/2019RG000678
- 899 Smith, C. J., & Forster, P. M. (2021). Suppressed late-20th century warming in  
 900 cmip6 models explained by forcing and feedbacks. *Geophysical Research Let-*  
 901 *ters*, *48*. doi: 10.1029/2021GL094948
- 902 Smith, D., Booth, B., Dunstone, N., Eade, R., Hermanson, L., Jones, G. S., ...  
 903 Thompson, V. (2016). Role of volcanic and anthropogenic aerosols in the  
 904 recent global surface warming slowdown. *Nature Climate Change*, *6*, 936–940.  
 905 doi: 10.1038/nclimate3058
- 906 Smith, D., Gillett, N. P., Simpson, I. R., Athanasiadis, P. J., Baehr, J., Bethke, I.,  
 907 ... Ziehn, T. (2022). Attribution of multi-annual to decadal changes in the cli-  
 908 mate system: The large ensemble single forcing model intercomparison project  
 909 (lesfmp). *Frontiers in Climate*. doi: 10.3389/fclim.2022.955414
- 910 Soden, B. J., & Held, I. M. (2006). An assessment of climate feedbacks in coupled  
 911 ocean–atmosphere models. *Journal of Climate*, *19*, 3354–3360. doi: 10.1175/  
 912 JCLI3799.1
- 913 Soden, B. J., Held, I. M., Colman, R., Shell, K. M., Kiehl, J. T., & Shields, C. A.  
 914 (2008). Quantifying climate feedbacks using radiative kernels. *Journal of*  
 915 *Climate*, *21*, 3504–3520. doi: 10.1175/2007JCLI2110.1
- 916 Stephens, G. L., Kahn, B. H., & Richardson, M. (2016). The super greenhouse effect  
 917 in a changing climate. *Journal of Climate*, *29*, 5469–5482. doi: 10.1175/JCLI  
 918 -D-15-0234.1
- 919 Titchner, H. A., & Rayner, N. A. (2014). The met office hadley centre sea  
 920 ice and sea surface temperature data set, version 2: 1. sea ice concentra-  
 921 tions. *Journal of Geophysical Research: Atmospheres*, *119*, 2864–2889. doi:  
 922 10.1002/2013JD020316
- 923 van der Dussen, J. J., de Roode, S. R., Gesso, S. D., & Siebesma, A. P. (2015). An  
 924 les model study of the influence of the free tropospheric thermodynamic condi-  
 925 tions on the stratocumulus response to a climate perturbation. *Journal of Ad-*  
 926 *vances in Modeling Earth Systems*, *7*, 670–691. doi: 10.1002/2014MS000380
- 927 Vial, J., Dufresne, J. L., & Bony, S. (2013). On the interpretation of inter-model  
 928 spread in cmip5 climate sensitivity estimates. *Climate Dynamics*, *41*, 3339–  
 929 3362. doi: 10.1007/s00382-013-1725-9
- 930 Webb, M. J., Lock, A. P., & Ogura, T. (2024). What are the main causes of posi-  
 931 tive subtropical low cloud feedbacks in climate models? *Journal of Advances in*  
 932 *Modeling Earth Systems*, *16*. doi: 10.1029/2023MS003716
- 933 Williams, K. D., Copsey, D., Blockley, E. W., Bodas-Salcedo, A., Calvert, D.,  
 934 Comer, R., ... Xavier, P. K. (2017). The met office global coupled model  
 935 3.0 and 3.1 (gc3.0 and gc3.1) configurations. *Journal of Advances in Modeling*  
 936 *Earth Systems*, 357–380. doi: 10.1002/2017MS001115
- 937 Wills, R. C. J., Dong, Y., Proistosescu, C., Armour, K. C., & Battisti, D. S. (2022).

938 Systematic climate model biases in the large-scale patterns of recent sea-  
939 surface temperature and sea-level pressure change. *Geophysical Research*  
940 *Letters*, *49*. doi: 10.1029/2022GL100011  
941 Zelinka, M., Zhou, C., & Klein, S. A. (2016). Insights from a refined decompo-  
942 sition of cloud feedbacks. *Geophysical Research Letters*, *43*. doi: 10.1002/  
943 2016GL069917